

# Remote Sensing of Volcano Surface and Internal Processes Using Radar Interferometry

Howard A. Zebker, Falk Amelung, and Sjlonni Jonsson

*Departments of Geophysics and Electrical Engineering, Stanford University, Stanford, California*

We describe here the use of imaging radar interferometry for remote sensing studies of volcanoes. Interferometric radars measure topography precisely, map surface cover changes such as active lava flows, and resolve extremely small deformations of the surface over large areas. First we present a tutorial on the radar interferometry technique. We then describe how these detailed measurements of surface processes may be further analyzed to infer volume or other changes at depth and thus provide a window through which to view subsurface activity. Because the subsurface transport of magma within a volcano is an important indicator of potential (or ongoing) activity, the ability to monitor deformations when they are slow or small, and often aseismic, could provide advance warning of future activity. Because radar measurements are not affected by clouds, radar is a valuable means to gather information in challenging, and even dangerous, environments spread over the entire Earth. In this chapter we present the technique of radar interferometry in a tutorial manner, give several example analyses of active volcanoes, and discuss its usefulness for the study of volcanoes in a variety of environments.

## VOLCANO STUDIES USING SATELLITE RADAR INTERFEROMETRY—AN INTRODUCTION

Understanding volcanoes and their interaction with the Earth's environment is important for many reasons. For one, volcanic activity is indicative of processes occurring far below the visible surface of the Earth. Another is that emission of gas or particulate material into the atmosphere can affect climate on a local, or even global, basis if an exceptionally large eruption occurs. Not least, volcanic activity is of considerable interest to those living on or near it, and planning for potential hazards relies on a full assessment of the likelihood of the various potential eruptive styles and their consequences.

Remote Sensing of Active Volcanism  
Geophysical Monograph 116  
Copyright 2000 by the American Geophysical Union

Radar interferometry provides a new tool aiding remote sensing studies of volcanoes. This imaging technique can examine in detail the topography of a volcano, map changes on its surface due to lahars, lava and pyroclastic flows, and, most excitingly, can discern subtle crustal deformation over wide areas, at high resolution, and without the use of on-site equipment or personnel. The development of interferometric radar systems for the highly accurate measurement of crustal deformation and surface topography has by now been well-documented in the literature [Graham, 1974; Zebker and Goldstein, 1986; Gabriel et al., 1989; Zebker et al. 1992; Evans et al., 1992; Massonnet et al., 1993; Gatelli et al., 1994; Zebker et al., 1994a, b]. The precision of the technique is now commensurate with conventional field survey and even GPS procedures [Madsen et al., 1995; Amelung et al., 1999], given that certain surface conditions exist. In addition, because the radar signals easily penetrate even dense clouds in the atmosphere and are independent of solar illumination, there

are also far fewer restrictions on data acquisition times and geometries from either airborne or spaceborne platforms using optical remote sensing instruments.

Radar interferometry promises to advance the study of volcanoes for several reasons. A satellite's global accessibility permits study of many volcano types in many different environments. Also, there is no need for pre-existing ground control information, unlike for conventional surveying techniques including GPS, leveling, EDM, and tilt meters. Thus, we do not need to predict before eruption which of the hundreds of potentially dangerous volcanoes might become active, given that a large number of volcanoes are visited by the satellite regularly and the data saved for future analysis. As a consequence, it lessens the need for ground crews to collect the needed data in dangerous areas; in the past two decades, numerous volcanologists have died attempting to collect data on active volcanoes. Here we describe some of the successes achieved to date with the interferometric technique, and we also illustrate why it has not yet been possible to realize all of the potential advantages. Further examples of this technique are provided by *Massonnet and Sigmundsson* [this volume].

Radar interferometry has been used, in one example, to investigate the relationship between lava production and overall volume change at Mt. Etna during a recent eruptive cycle [*Massonnet et al.*, 1995; *Lanari et al.*, 1998]. Similar change detection at this and other volcanoes could warn of impending eruptions in advance, minimizing loss of life and perhaps lessening an eruption's impact on property. Radar also provides unique observations of active surface processes on volcanoes. For example, the SIR-C radar has been used to map the evolution of active lava flows on Kilauea volcano by determining the daily area of surface decorrelation over a period of four successive days in 1994 [*Zebker et al.*, 1996]. The ability to determine flow rates and volumes helps not only in understanding the eruptions from a scientific standpoint, but also could be used for hazard mitigation and operational data if acquisitions were frequent and comprehensive. Radar observations can, in addition, be reduced to topographic data, themselves very useful in many volcanic characterizations. Topographic measurements in principle can monitor the growth of potentially unstable lava domes, such as have occurred in the 1990s on Montserrat and Mount Unzen.

The most promising use of radar analysis for volcano hazards is the detection of pre-eruptive ground deformation from the intrusion of magma into a magma chamber or into smaller cracks within the crust. Although uplift from ascent of magma into the shallow crust has been observed

prior to some eruptions, particularly on basaltic shield volcanoes, little is known in detail about the rate or spatial extent of this deformation on most of the world's volcanoes because few are monitored regularly. Those that are monitored are in addition sampled spatially only very coarsely, so that unaliased, precise solutions for the subsurface activity are not possible. For example, crustal deformation in the vicinity of the caldera itself has been 600 mm since 1979 [*Langbein et al.*, 1993], with the rate of uplift over the past five years increasing to 20-40 mm yr<sup>-1</sup>. Potential hazards associated with the Long Valley Caldera and many other volcanoes throughout the world, imply that deformation monitoring with interferometric radar is an essential complement to conventional geodetic measurements [*Thatcher and Massonnet*, 1997]; these results were extended to infer magma chamber parameters and other geodetic data by Simons in 1998 (M. Simons, personal communication, 1999). Such analyses with their improved model constraints will impact our ability to forecast impending eruptions [*Dixon*, 1994].

Some internal volcanic processes, such as the emplacement of dikes and sills, involve intrusion of magma between layers of rock; others concern transport of water or gas underground. The resulting displacements at depth are hidden from our direct view, but they often slightly distort the surface enough to be detectable by precise measurements. Several techniques possess a level of sensitivity to measure these deformations, including leveling, tilt meter, or, more recently, GPS measurements, but none of these typically resolves the deformation field spatially with enough acuity to permit detailed comparison of the many possible subsurface deformation models. Radar interferometry provides deformation measurements at a spatial resolution of 10's of meters, over areas 100's of kilometers in size, at a precision of 1 cm or less under certain conditions, leading to detailed models of magma movement or pressure change below ground.

In this chapter we describe the radar approach, examine its limitations, and present some illustrative results of its application to presently active volcanoes. We illustrate several descriptors of volcanoes and volcanic activity, including topographic data, measurements of flow rates and volumes, and most importantly, deformation of active volcanoes. Finally we examine where we are today in applying interferometry to volcanoes of different types in different environments. Additional discussion on specific problems associated with viewing geometry, and the selection of data sets suitable for interferometric analysis, is presented by *Massonnet and Sigmundsson* [this volume].

## A RADAR INTERFEROMETRY TUTORIAL

Radar is an instrument for measuring distance. In its simplest form, a radar operates by broadcasting a pulse of electromagnetic energy into space. If that pulse encounters an object then some of that energy is redirected back to the radar antenna. For example, airport radar landing systems work in this simple manner. Pulses of radiation are transmitted from an antenna near the airport and echoes are received from any aircraft in the area. Precise timing of the echo delays allows determination of the distance, or "range", to the aircraft to an accuracy of meters, because the velocity of propagation is known.

The same echo delay technique can be used to map the ground surface if the transmitter and receiver are mounted on board an aircraft or spacecraft and the antennas are directed downward. In this configuration the energy received from many points on the surface is separated by the times required for the transmit pulse to travel to various locations on the surface and return to the radar. As the platform moves along an orbit or flight track a "swath" is swept out along the surface and many measurements are combined to form an image of the radar reflectivity of the ground. Many techniques exist for improving the resolution of these basic measurements—using pulse compression and synthetic aperture radar (SAR) algorithms resolutions of a meter or less can be achieved using spaceborne instruments. Typical systems used in geophysical applications attain a resolution of about 10-20 m in the across-track, or range, direction, and 4-5 m in the along-track, or azimuth, direction.

For radar interferometry, images obtained by two antennas displaced in time, space, or both are compared. Suppose we obtain two such radar images of a region on the surface of the Earth. These two images may result from two "passes" of the radar platform over the same ground area displaced in time or received simultaneously from two separate antennas displaced spatially. We refer to the spatial displacement of the sensors as a "baseline" and the temporal displacement as the repeat interval. The images will resemble one another, each being a map of the radar reflectivity of nearly the same ground surface. Any distortion of the surface from motion between observations will be revealed as shifts in location of ground points in the images. Similar shifts in position of points in the image result from a change in viewing angle, a parallax effect that can be exploited to deduce topography.

If, for example, two radar images are acquired on successive orbits of a radar satellite, and the ground has

shifted between observations such as can happen owing to intrusion of magma into a magma chamber, these displacements can be measured by comparing the offsets between the images at each point on the surface (Plate 1). Alternatively, if the two images are acquired from slightly different positions in space then the viewing parallax causes the images to be slightly distorted versions of each other, even if there has been no ground motion. In this case the distortion is dependent on the surface topography. This is analogous to stereo-imaging that is commonly used to measure topography, except that the data are radar rather than optical images and the geometry of acquisition is somewhat different. We note that parallax is necessary to resolve topography, but for the measurement of deformation parallax in viewing is not required and even degrades the observation.

The above hold even in the case of optical images, as well as for radar instruments. But radar offers a distinct advantage in measurement of the displacements of the ground points: it can be thousands of times more accurate. This advantage follows from the "coherent" nature of radar sensors, that is, the signal phase, not only its brightness, is observed (Plate 2). This attribute allows us to measure distances to a small fraction of the illumination wavelength, as opposed to the resolution limit in intensity systems. So although the spatial resolution of a radar system may be 10 m or so, distortions in the images may be determined to millimeter level for wavelengths of several centimeters, albeit at postings on the ground determined by the resolution value. In the next section we present a quantitative discussion of exactly how such a system may be implemented.

### *Quantitative Theory*

In this section we derive the equations needed for calculating ground displacement fields or surface topography from interferometric synthetic aperture radar measurements. Here we assume that the reader has a general knowledge of radar remote sensing systems. The interested reader may consult a general text on radar remote sensing (e.g., *Elachi* [1988] or *Curlander and McDonough* [1991]) for questions on radar system operation and processing. As for information on the technique of radar interferometry, much of the work is still too new for general textbooks and thus the technical literature is the only source available.

A side-looking spaceborne synthetic aperture radar system may map a continuous swath many tens of kilometers

in width as the satellite progresses along its orbit track, yielding measurements of the amplitude and phase of radar echoes associated with independent patches on the ground perhaps 10 m in size; this size is the resolution of the radar. Suppose two images of the same ground surface are acquired; differencing these in phase forms an interferometer and the difference image is called an interferogram. We first examine the case where the radar is located at precisely the same location in space observing the identical ground area, but that some distribution of ground movement between radar observations occurs. The measured phase at each point in each of the two radar images is related directly to the distance traveled by the signal, and may be taken as equal to the sum of a propagation part proportional to the round-trip distance traveled and a scattering part due to the interaction of the wave with the ground. If each resolution element on the ground behaves the same for each observation (we will discuss more regarding this important condition below), then calculating the difference in the phases removes dependence on the scattering mechanism and gives a quantity dependent only on any displacements of the surface between observations. If the two path lengths are taken to be  $\rho$  and  $\rho + \delta\rho$ , with  $\delta\rho$  the radar line-of-sight displacement of the surface between observations, the measured phase difference  $\phi$  at wavelength  $\lambda$  is called the interferometric phase and will be

$$\phi = -(4\pi/\lambda)\delta\rho \quad (1)$$

or  $2\pi$  times the round-trip distance difference in wavelengths. Thus creating an image of the phase differences produces a map of ground displacement in the direction of the radar line-of-sight.

But it is quite difficult in practice to ensure that the radar platform returns to exactly the same position for the second observation. This is beyond the limits of navigation as currently available, so we must settle for returning only approximately to the same position. Hence the surface will be viewed from a position near the initial position, resulting in some parallax distortion in every interferogram, as described above. We note that it is this additional displacement that is invertible to recover topography from an interferogram.

We quantify the added parallax distortion as follows. Let the two antenna locations be no longer coincident; displace them spatially to occur at positions A1 and A2 (see Figure 1). Because of the difference in viewing direction, even in the absence of ground motion we will observe a displacement  $d\rho$  that is dependent on viewing geometry and surface topography. The total displacement now consists of two parts:  $\delta\rho$  for the real surface motion between

observations, and  $d\rho$  for the apparent motion due to parallax. The law of cosines permits solution for the total displacement  $d\rho + \delta\rho$  in this case as follows. We have

$$(\rho + d\rho + \delta\rho)^2 = \rho^2 + B^2 - 2\rho B \sin(\theta - \alpha) \quad (2)$$

where the baseline length is  $B$ , the range to the point on the ground in the first image is  $\rho$ , the look angle is  $\theta$ , and the angle of the baseline with respect to horizontal at the sensor is  $\alpha$ . Neglecting the term of order  $(d\rho + \delta\rho)^2$  yields

$$d\rho + \delta\rho \approx \left( \frac{B^2}{2\rho} \right) - B \sin(\theta - \alpha) \quad (3)$$

Since  $\rho$  is usually much larger than  $B$ , we can neglect the first term on the right hand side of (3), although it is not necessary for the analyses presented below. In this case we obtain

$$d\rho + \delta\rho \approx -B \sin(\theta - \alpha) \quad (4)$$

or, considering the case for topography only, with no actual ground displacement,

$$d\rho \approx -B_{||} \quad (5)$$

Topographic sensitivity of the instrument enters through the dependence of the exact look angle  $\theta$  on the elevation  $z = h - \rho \cos \theta$ , where  $h$  is the height of the sensor above the reference surface. Thus we may use the interferometric measurement to determine topography of the surface, often itself a valuable descriptor of a volcano. Note that  $B_{||} = -B \sin(\theta - \alpha)$  is simply the component of the baseline parallel to the look direction. This is the parallel-ray approximation used by Zebker and Goldstein [1986] in their initial paper on topographic mapping.

Equations (1)–(5) show that the measured phase of an interferometer in wavelengths is the component of the interferometer baseline parallel to the look direction to a given point on the surface measured in wavelengths, plus any real surface displacement, multiplied by two for round-trip travel.

Because an interferogram contains phase variations dependent on both topography and on surface deformation, these effects must be separated if we are to interpret the interferograms unambiguously.

The topographic phase signature can be removed from an interferogram if a pre-existing digital elevation model (DEM) exists (sometimes referred to as the two-pass method), or if a second interferogram containing topographic signal only is acquired (the three- or four-pass method). The two-pass method was initially developed by

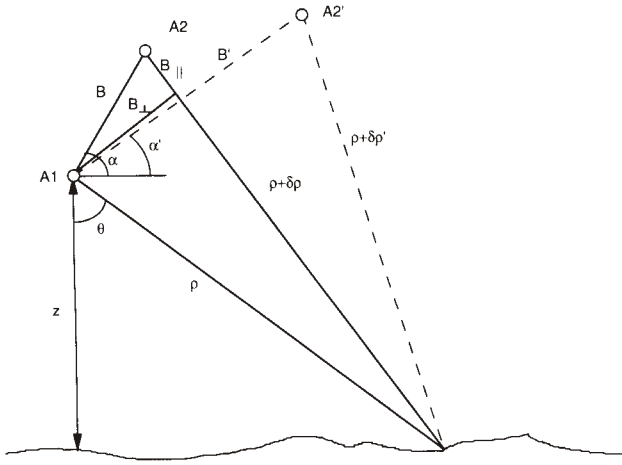


**Figure 1.** Interferometer imaging geometry. Radar antennas A1 and A2 both illuminate the same patch of ground centered at  $y=0$ . Incidence angles  $\theta_1$  and  $\theta_2$  result in phase offsets for all points P displaced by distance  $y$  of  $y \sin \theta_1$  and  $y \sin \theta_2$ , respectively. Difference of these phases is measured interferometer phase. A third pass (dashed lines) permits separation of the topographic and deformation signatures. Note that the distance to the ground  $\rho$  is much larger than  $B$ , hence the two antenna positions are virtually coincident. Nonetheless, the precision of the interferometric technique allows the difference in path length to be determined to a small fraction of a wavelength.

*Massonnet et al.* [1993] at CNES Toulouse, is implemented by calculating explicitly the expected interferogram assuming no ground displacements. This interferogram is then subtracted in phase from the measurements (as represented in equation (4)), leaving a phase signature that is dominated by any real displacement effects. In this approach accuracy will be limited by the precision of the DEM. Usually DEM accuracies are satisfactory if the posting is better than 100 m and the precision is better than 10 m, although this depends somewhat on imaging geometries (see error effects below).

Specifically, the synthetic interferogram is calculated from the topography and viewing geometry using equations given above, in the form

$$\phi_{synthetic} = -\frac{4\pi}{\lambda} B \sin\left(\cos^{-1}\left(\frac{h-z}{\rho}\right) - \alpha\right) \quad (6)$$

where  $h$  is the sensor altitude and  $\alpha$  is the angle of the interferometric baseline with respect to horizontal. This phase is subtracted from the interferogram on a pixel by pixel basis, leaving only the signature of the deformation. We note that for the derivations shown here, we assume

that the Earth's surface is flat, not curved. Similar expressions using a curved surface may be derived with some algebra and geometry with the result that the equations are somewhat more complicated. In the case of spaceborne sensors, the flat-Earth approximations will usually not be accurate enough for geophysically useful results.

The three- or four-pass method was first described by *Gabriel et al.* [1988] and applied to the measurement of coseismic deformation by *Zebker et al.* [1994b]. In this method, a third radar image is used, forming a second interferogram with one of the initial pair of images (dashed lines in Figure 1), or a second pair entirely forms the reference interferogram. For instance, if the repeat interval for one of the interferograms is one day, and that of the second is one year, we would expect that the deformation observable in the short time interferogram is small. The same topographic signature would be present in both. For a volcano, if one pair spans an eruption and the other is acquired over a quiescent period, the former would be assumed to have the deformation signal while the latter would not.

Let us denote the interferogram with no expected deformation as the “topography” interferogram  $\phi_t$ , and the other interferogram as the “deformation” interferogram  $\phi_d$  reflecting which effect will dominate the phase signature. In fact the second interferogram will possess both topographic and deformation signatures, but in many cases the deformation signature will truly be larger. It may seem counter-intuitive that centimeter-level displacements would possess a larger phase signal in the interferogram than topography, but the sensitivity analysis presented later shows that the sensitivity to topographic change can be thousands of times greater than the sensitivity to topography itself.

The second interferogram is acquired over the same area as the first, sharing one orbit with the previous image pair so that  $\rho$  and  $\theta$  are unchanged. Denoting all quantities related to the topographic interferogram by the subscript  $t$  and those describing the deformation interferogram by the subscript  $d$ , we can compare the interferogram phases. The topographic interferogram is acquired with a different baseline  $B_t$  and baseline orientation  $\alpha_t$ , thus a different  $B_{\parallel t}$ . Combining (1) and (5) above we obtain

$$\phi_t = -\frac{4\pi}{\lambda} B_{\parallel t}. \quad (7)$$

In the absence of surface displacements, examination of the ratio of the two phases yields

$$\frac{\phi_d}{\phi_t} = \frac{B_{\parallel d}}{B_{\parallel t}}, \quad (8)$$

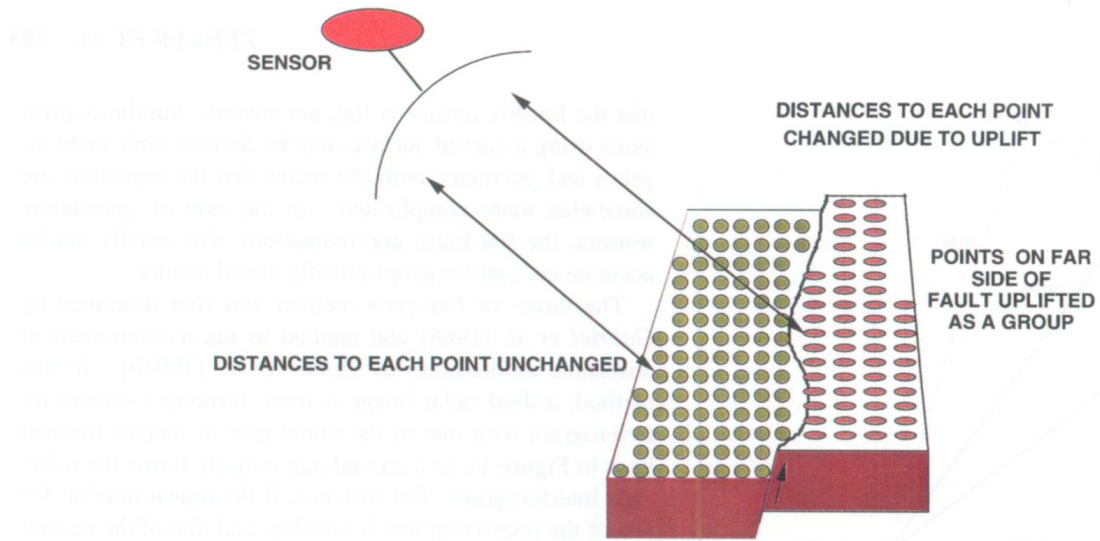


**Plate 1.** Measurement of displacement using imaging radar interferometry. The imaging system determines the distance to all points in an image, and those that have been displaced, as these across a fault, will be seen as phase shifted in the radar interferogram.

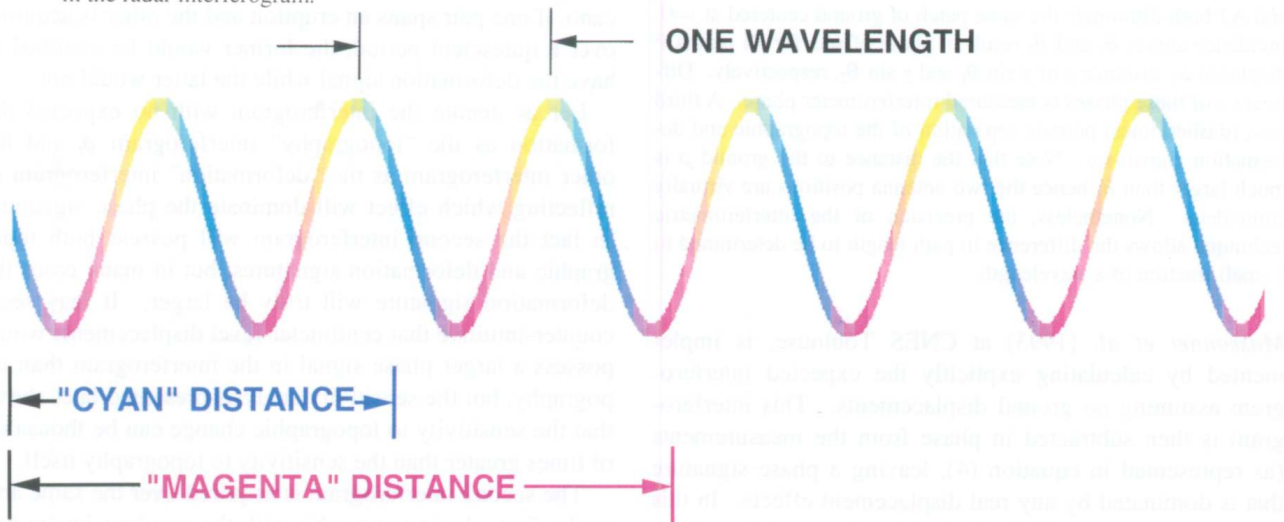


**Plate 2.** Illustration of measuring the phase of a radar signal. The phase repeats each cycle of the electromagnetic wave and in interferograms is often displayed as a color that advances and repeats with increasing distance. Phase is assumed to be proportional to distance at the wavelength scale. Interferometry allows the precise measurement of the phase of the reflected radar signal, permitting a precision of a small fraction of the radar wavelength to be realized.

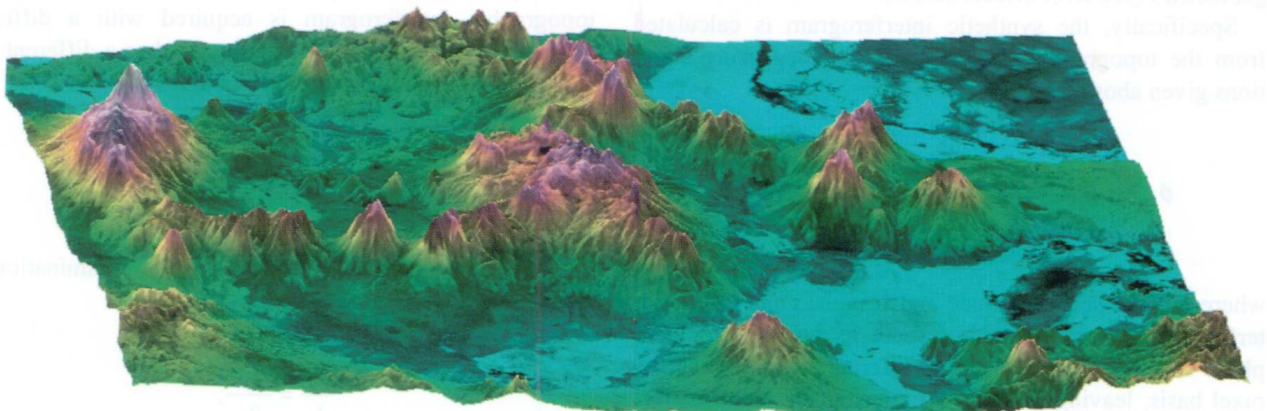


**Plate 3.** ERS-1 interferometric digital elevation model of Irruputuncu volcano in northern Chile.

In other words the ratio of the phases is equal to the ratio of the parallel components of the baseline. Thus we can use the solution from the topography interferogram to remove the topographic phase term from the deformation interferogram. Specifically we combine the two interferogram phases and isolate the deformation signature, as

$$\phi_d - \frac{B_{\parallel d}}{B_{\parallel t}} \phi_t = -\frac{4\pi}{\lambda} \delta\rho. \quad (9)$$

Since the quantity on the left is determined entirely by the phases of the interferograms and the orbit geometries, the line of sight component of the displacement  $\delta\rho$ , is measurable from the phase at each point in the scene.

The ratio

$$\frac{B_{\parallel d}}{B_{\parallel t}} = \frac{B_d \sin(\theta - \alpha_d)}{B_t \sin(\theta - \alpha_t)} \quad (10)$$

is a function of the angle  $\theta$ , which depends both on the illumination geometry and also the topography at each point in the radar image. To evaluate (9) via (10) directly, we must again know the topographic map of the area of interest, either from the interferometric data or from the elevation data in another source. But there is an indirect approach for which it is not necessary to implement the step of either topographic solution or registration of dissimilar data sets, leading to simplicity and accuracy in the three-pass solution.

The approach is to remove from the interferogram phase a term that would exist even in the absence of topography on a flat, or perhaps spherical, earth. The phase corrected for the "flat Earth" (or "curved Earth" where the curvature is important) effect, denoted  $\phi_{flat}$ , is given by

$$\phi_{flat} = -\frac{4\pi}{\lambda} |B \sin(\theta - \alpha) - B \sin(\theta_0 - \alpha)| \quad (11)$$

where  $\theta_0$  is the look angle to each point in the image assuming zero local height. The interferogram phase after this correction represents the distortion of the interference grating pattern due to topographic variation relative to a spherical surface and assuming no displacements due to motion in the scene. Many interferograms shown throughout the literature have been "flattened" according to equation (11), otherwise there would be a high-rate fringe pattern confusing the images.

Noting that the deviation of the exact  $\theta$  from  $\theta_0$  is small, we can expand the first term on the right hand side of (11), leading to

$$\phi_{flat} = -\frac{4\pi}{\lambda} \delta\theta B \cos(\theta_0 - \alpha) \quad (12)$$

where  $\delta\theta = \theta - \theta_0$ . Numerically,  $\phi_{flat}$  is equal to the product of the perpendicular component of the baseline  $B_\perp$ , assuming no topography is present on the surface, and the topographic angular distortion  $\delta\theta$ . Thus, the ratio  $\phi_{flat,d}/\phi_{flat,t}$  is now in terms of  $\theta_0$  rather than  $\theta$  and depends only on the viewing geometry and the baseline. If we now restate the differential phase equation (9) above in terms of the flattened phase  $\phi_{flat}$ , we obtain

$$\phi_{flat,d} - \frac{B_{\perp d}}{B_{\perp t}} \phi_{flat,t} = -\frac{4\pi}{\lambda} \delta\rho \quad (13)$$

With this function, we can now solve directly for the displacement  $\delta\rho$  without requiring the exact values of  $\theta$ , and hence the topographic information, at an intermediate step.

If the baseline used in the flattening operation (equation 11 above) is not exactly the true baseline value, equation (13) will contain error terms and the subsequent displacement maps will be distorted. Similarly, if the wrong baseline is used in equation (6) to derive the synthetic interferogram, the displacement maps will be in error. Thus in both the two-pass and three-pass methods some knowledge of the interferometer baselines is required.

We have shown that the phase in radar interferograms depends both on the local topography and also on any motion that may occur between viewing instances. That the interferograms are sensitive to meter level changes in topography but millimeter or centimeter level changes in displacement may be seen if we compare the sensitivity of the phase measurement to each phenomenon. We differentiate (7) with respect to topography (through  $B_\parallel$ ) and (9) with respect to displacement. In the first case, using  $dz = \rho \sin\theta d\theta$ , obtained from the dependence of height on angle described above, we find

$$d\phi = -\frac{4\pi}{\lambda} B \cos(\theta - \alpha) d\theta \quad (14)$$

and

$$\frac{d\phi}{dz} = -\frac{4\pi}{\lambda} \frac{B \cos(\theta - \alpha)}{\rho \sin\theta}. \quad (15)$$

For the displacement case we have

$$\frac{d\phi}{d\delta\rho} = -\frac{4\pi}{\lambda}. \quad (16)$$

Since the distance  $\rho$  typically is very much greater than the baseline distance  $B$ , it is evident from equations (15 and 16) that a much more sensitive dependence of phase results from deformation than from topographic variation.

In other words, the system is more sensitive in an absolute sense to surficial change than to the topography itself. Comparing the two results numerically, for a typical ERS viewing geometry one meter of topography gives a phase signature of  $4.3^\circ$ , while for the same pass pair a one meter surface displacement yields a phase signature of  $12800^\circ$ , or nearly 3000 times greater sensitivity. Thus, while radar interferometry can be used to measure topography to an accuracy of meters, displacements may be determined to the centimeter or millimeter level.

This ratio of sensitivities illustrates the power of the interferometric technique to detect small changes. If, for example, we chose to map volcanic displacements by differencing DEMs, whether acquired interferometrically or by conventional stereo photogrammetry, changes would only be visible if they were significant in size compared to the uncertainty of the DEM measurement (typically several meters). Because most spaceborne interferometers permit topographic mapping with a vertical precision of several meters (see Zebker *et al.*, 1994a for a discussion of ERS-1 DEMs with 4.6 m precision), a worthwhile result for many applications, their acuity is not particularly useful for the study of many volcanic deformations. In contrast, if data are acquired with an interferometric pair that spans an eruptive event, even 1 cm of line-of-sight displacement results in an easily-detectable signature of  $64^\circ$  for a C-band sensor such as ERS-1.

#### *InSAR Measurements as Constraints on Geophysical Parameters*

Until now we have discussed the use of radar interferometry for measuring surface processes and deformation fields. But if our principal interest in these data is to help understand processes at depth, we would like to interpret these surface displacements as surface expressions of dynamic processes beneath active volcanoes. For example, we might like to infer the dimensions of a subsurface dike intrusion or fault parameters of an earthquake dislocation, knowing only the measured surface deformation. Thus the next step in the analysis is to invert the observations to obtain a description of subsurface activity (see Figure 2). It must be noted that noise in the measurement leads to correlation between the set of parameters solved for, and thus some simplifying assumptions are needed regardless of the number of pixels in the original image interferogram.

For volcanic studies, we are interested in both the deformation fields due to dislocations beneath the volcano, such as from dike intrusions, and also due to pressure changes as modeled, for example, by Mogi sources (spherically symmetric pressure sources). In both cases we

frame the inverse problem as an integral equation relating the subsurface phenomenon to surface displacement using a Green's function formulation. For the dislocation source we might use the following forward integral giving displacements  $u(x)$  at location  $x$  owing to displacements across a dislocation surface  $\Sigma$ , as described by Volterra's formula:

$$u(x) = \iint_{\Sigma} \Delta u(x') G_{disp}(x', x) n(x') d\Sigma \quad (17)$$

where  $\Delta u(x')$  is the displacement across the surface  $\Sigma$ ,  $G_{disp}(x', x)$  is the Green's function relating surface displacements at  $x$  to a point force acting at  $x'$ , and  $n(x')$  is a unit normal to the dislocation surface. A closed analytical solution exists for surface displacements on a halfspace in the case of rectangular dislocation surface  $\Sigma$  embedded in the elastic halfspace [Okada, 1985]. Details of one solution for a dike emplacement under an active volcano are given in Jonsson *et al.* [1999]; a summary of the results are given below.

For a pressure source we might use instead this integral relating the change in pressure with time  $\Delta p(x, t)$  throughout a volume  $V$  to the observed time-varying surface displacement  $u(x, t)$ :

$$u(x, t) = \iiint_V \Delta p(x', t) G_{pres}(x, x') dx' \quad (18)$$

where now the Green's function relates surface displacements to pressure at  $x'$ . We note that Mogi sources would be treated using this form of the inverse equation.

There are many techniques for solving similar inverse problems. Usually the surface data are sparsely distributed, so that matrix representations of the forward problem are reasonably small in size, comprising measurements at tens or perhaps a few hundred locations. The difference in the radar case is that we obtain displacements at thousands or millions of points on the surface, thus making possible unprecedented numbers of solution parameters. For example, with all this extra data, we might solve for arbitrary dike shapes or thicknesses that vary with location. The cost for this additional freedom in modeling is that the matrices grow very large, and finding an optimal solution becomes a difficult numerical task. Inversion of very large matrices is generally prohibitive, so we have achieved some success averaging data to a somewhat coarser grid before inversion. This still results in vastly more data than we often have for conventional field measurements. In the example we show below, we used simulated annealing approaches to evaluate a global error minimum. But this averaging step is still time consuming and necessitates loss of

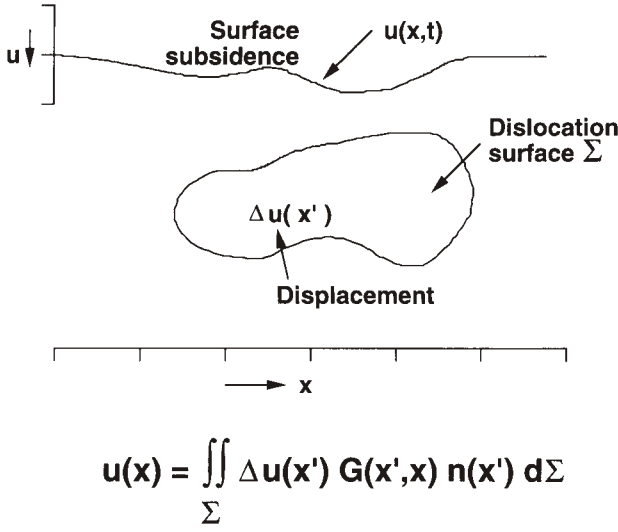


**Figure 2.** Illustration of how changes at depth distort the overlying surface, which we can measure directly. The subsurface and surface changes are related through integral equations incorporating the elastic properties of the Earth. The equation shown here relates the two using a Green's function formalism. Mathematical inversion procedures must be used to retrieve change at depth from the observed surface deformation.

potential detail, and avoiding these problems is the subject of much current research.

#### Limitations and Error Sources

There are, however, several important limitations to the interferometric technique. Recall that we modeled the radar echoes as possessing a phase that depended both on the distance traveled (the propagation part) and on details of the interaction with the surface (the scattering part). Changes to either of these will affect the observed interferograms, leading to mis-estimation of the displacements between the two images, or to unreliable, excessively noisy phase measurements.

Consider first the propagation term. In our derivation we assumed that any phase observed would be directly proportional to the physical distance from the radar to the ground. We generally assume that the signals propagate at known constant velocity to convert the time delays and phase shifts to distance. However, if the signals propagate through the spatially inhomogeneous Earth's atmosphere, which has a slightly higher index of refraction than free space, the velocity is lowered slightly, leading to spatially variable delays which contaminate the observations. The spatial variability is due to the variability of the atmosphere itself, including—most importantly—variation in water vapor distribution. Atmospheric variations can be

expected whenever the two images are not acquired simultaneously.

The magnitude of these distortions can be significant, leading to several centimeters of displacement error or 100's of meters of topographic error. We relate the errors in measurement to atmospheric conditions as follows. Propagation through the Earth's atmosphere takes slightly longer than propagation through free space, because the refractive index  $n(x)$  is greater than 1. Here the independent variable  $x$  gives location in space, and  $n(x)$  may vary vertically and horizontally. This extra time can be approximated as an extra distance of propagation  $\Delta x$  but with the wave traveling at the usual speed of light. Thus to each phase measurement above we must add an extra propagation phase

$$\phi_{prop} = -\frac{4\pi}{\lambda} \Delta x$$

and  $\Delta x$  itself may be expressed in terms of atmospheric parameters at the surface using the empirical formula [Saastamoinen, 1972]

$$\Delta x = \left| 2.277 \times 10^{-3} - 1.11 \times 10^{-5} \cos \Lambda \right| P_s + 2.277 \times 10^{-3} \left| 0.05 + \frac{1255}{T_s} \right| e_s \quad (20)$$

where  $P_s$  is the surface pressure in millibars,  $e_s$  is the surface partial pressure of water vapor in millibars,  $T_s$  is the surface temperature in Kelvins, and  $\Lambda$  is the latitude of the observing point.

If the atmosphere did not vary with time, then the extra path  $\Delta x$  would be the same on both observations and would disappear when the interferogram is calculated from the phase difference. But the parameters in (18) above do vary, spatially over the area imaged and also between observations. The most significant variation is in water vapor, which can be enhanced in volcanic regions as it is a common emission product. Temperature and dry pressure variations are much smaller and can usually be neglected. But generally multiple interferograms of an area must be compared to identify small surface deformations as real and not as atmospheric artifacts. The effects of atmosphere on interferograms are described in detail by Zebker *et al.* [1997].

A second major limitation results from changes to the scattering part of the signal phase. We have until now assumed that the interaction of the radar waves with the surface is exactly repeatable between measurements. If the ground is completely undisturbed between observations

then this will indeed be the case, however all natural surfaces vary with time. In some cases this variation is negligible, and the scattering phase will essentially cancel during formation of the interferogram. But if the surface is vegetated, or weathers appreciably, or if snow or other groundcover changes, then the scattering phases can change dramatically. This gives rise to temporal decorrelation, which is the loss of interferogram coherence with time. Volcanoes are often quite changeable environmentally, and obtaining high-quality interferograms can be challenging for many locations. We will present in a later section some sample interferograms of volcanoes in different parts of the world to demonstrate the variability in correlation.

Other changes also affect the scattering phase. The same parallax effects that allow us to measure topography also distort the radar echo at the sub-pixel level and cause spatial decorrelation. In fact these lead to a maximum difference in look angle, corresponding to a maximum baseline, beyond which no reliable phase estimate will result. Several studies have addressed this phenomenon, both theoretically [for example, *Li and Goldstein, 1990*], and experimentally [for example, *Gray and Farris-Manning, 1993*]. *Zebker and Villasenor [1992]* were able to model and quantify a number of decorrelation sources, including some temporal decorrelation processes, and found that different surfaces decorrelate at different rates. This limits the applicability of the approach to areas that do not change much with time. Some regions, such as desert areas, may exhibit very little decorrelation over long periods. Interferograms of years in extent have been presented in the literature.

The limits on baseline depend on radar parameters as well as viewing geometry. Some of the more useful equations [*Zebker and Villasenor, 1992*] in selecting interferometric-quality data sets are (i) the critical baseline

$$B_c = \frac{\lambda p}{2R_y \cos^2 \theta} \quad (21)$$

where  $R_y$  is the range resolution and (ii) the relation between sub-pixel scatterer motions across-track and vertically (given by variances in position  $\sigma_y^2$  and  $\sigma_z^2$ , respectively) and temporal correlation  $\rho_{temporal}$ :

$$\rho_{temporal} = \exp \left\{ -\frac{1}{2} \left( \frac{4\pi}{\lambda} \right)^2 (\sigma_y^2 \sin^2 \theta + \sigma_z^2 \cos^2 \theta) \right\} \quad (22)$$

As an example, for ERS-1 and -2, the critical baseline is 1200 m, and the amount of random motion that can be tolerated before losing correlation completely between observations is about 3 cm. These can guide selection of interferometric-quality passes from tables of both orbital parameters and times of acquisition.

The spatial distribution of correlation measurements itself can be of great use in interpreting interferometric data acquired over active volcanoes. We will illustrate below one such application, in which the areal coverage of active lava flows is recorded each day, giving estimates of flow rates and lava volumes. This follows from the complete decorrelation of the echoes if a region is covered by a new flow, as the individual scatterers that formed the echo on the first pass are invisible to the radar on the second pass, leading to no significant relation in the two signals.

A third limitation, important for all three-pass and some two-pass implementations, is that the phases must often be "unwrapped" to achieve the greatest accuracy in displacement phase estimation. The measurements of each phase are known only modulo  $2\pi$ , and various techniques exist [*Goldstein et al., 1988; Ghiglia and Romero, 1994; Zebker and Lu, 1998*] to determine the absolute phase relationship between all arbitrary points in a data set. The ability to unwrap arbitrary phase fields depends on several factors, including the noise level in the system and the interferometric fringe spacing. Since the fringe rate depends on local surface slope, typically it is more difficult to estimate phases reliably in rough terrain than in flat terrain if the fringe rate is high to begin with. The result of this is that we will be unable to obtain reliable phase estimates in the roughest regions, such as when the surface slope is comparable to the radar look angle.

## EXAMPLES OF INTERFEROMETRIC RADAR APPLICATIONS TO VOLCANO STUDIES

In this section we present several examples of the application of interferometric radar techniques to the study of volcanic processes. We present examples of (i) topographic reduction of volcanic features, (ii) using the variations in correlation to measure lava flow rates and volumes, and (iii) an inversion of deformation data to infer parameters of a shallow dike emplaced during a recent eruption.

### *Topography*

Knowledge of the topography of a volcano is helpful both in characterizing evolutionary models and in determining hazard potential. The shape of a volcano tells

Table 1. TOPSAR and ERS-1 Radar System Parameters

Parameter	TOPSAR	ERS-1
Wavelength, m	0.0566	0.0566
Peak power, watts	1000	4800
Pulse rate, Hz	600 nominal	1679 nominal
Pulse length, $\mu$ sec	5.0	37.1
Antenna length, m	1.6	10
Antenna width, m	0.11	1
Antenna gain, dB	25	43.2
Range bandwidth, MHz	40	15.55
Receiver noise temperature, K	2100	3700
Antenna baseline, m	2.58	Variable
Baseline angle ( $\alpha$ ), deg	62.77	Variable
Slant range resolution, m	3.75	9.6
Azimuth resolution, m	1.2	6.5
Platform altitude, km	8	790
Look angle, deg	20-65	23
Repeat interval, days	N/A	3, 35, 165

much about the processes that formed it, and also contains much of the past history of the eruption in surfaces of varying ages. Accurate DEMs are of great use in predicting the paths of potential lahars or pyroclastic flows, and can be used to develop detailed hazard potential maps [see, for example, *Iverson et al.*, 1998], as well as permit detailed geomorphic studies of volcanoes [*Rowland and Garbeil*, this volume]. In this section we show examples of topographic data acquired by the ERS-1 radar satellite operating in a repeat pass mode and also by the TOPSAR airborne prototype topographic radar. These serve as case studies of the capabilities of existing systems commonly used by geoscientists today. The hardware characteristics of these systems are compared in Table 1.

The ERS-1 and -2 satellite synthetic aperture radars possess the advantages listed above in its ability to acquire topographic data on volcanoes worldwide. We can illustrate a sample DEM derived from ERS using data acquired over a volcanic region including Irruputuncu volcano in northern Chile. Plate 3 is derived from tandem mission ERS data with a repeat interval of one day, minimizing temporal decorrelation and with the two orbits separated by about 100 m in space. This image is 80 km on a side, and represents a subset of a single swath of radar data.

While we have not completed a detailed performance analysis of this scene, 5 m vertical precision is probably a good estimate based on previous studies of DEMs derived from ERS [*Zebker et al.*, 1994a]. The main factors affecting topographic mapping performance are baseline length, baseline knowledge, and temporal decorrelation of the surface. For ERS-1 and -2 the critical baseline is 1200 m, and best performance in practice is realized for a baseline length near 200 m. ERS-1 has been operating in a 35-day repeat cycle for several years and fortunately many revisits

to a site have been possible, so that for many different volcanoes nearly optimal data are available. Derivation of a DEM requires selecting a pair from the set of available data with a usable baseline.

However, for some volcanoes the sides are so steep as to cause the image to be layed-over in ERS data, while for others severe environmental conditions leads to poor data quality from temporal decorrelation effects. For some of these volcanoes we instead can use data acquired by the airborne TOPSAR system, which has advantages over ERS of higher resolution, no temporal decorrelation, and greater look angles which imply less layover. The TOPSAR system is implemented on a NASA DC-8 aircraft. Since two antennas are implemented on the aircraft, data are acquired simultaneously and there is no temporal decorrelation. This radar also operates at C-band and has somewhat higher performance in terms of signal to noise ratio and resolution as compared to the spacecraft system. However, the swath width is only 10 km in contrast to the 100 km swath imaged by ERS.

An example of an airborne radar interferometer DEM is shown in Plate 4, a contour map derived from TOPSAR data over the Galapagos island of Fernandina. The Galapagos archipelago is located on the Nazca plate about 1000 km west of Ecuador, just south of the east-west trending Galapagos spreading center. The islands are a cluster of about 20 basaltic volcanoes with large summit calderas. Fernandina Island is about 30 km in diameter and consists of a single volcano with a maximum elevation of 1470 m with a nearly 1000 m deep central caldera. Fernandina is among the most active volcanoes in the world; it erupted at least 13 times during 1950-1998 [*Rowland and Munro, 1992*]. The most recent activity at Fernandina includes intra-caldera eruptions in 1988 and 1991, and a radial fissure eruption in 1995 that we will describe more later. *Rowland* (1996) used the TOPSAR data to infer surface slopes, lava flow volumes, and vent distributions on Fernandina.

#### Lava Flow Rates and Volumes

In this section we illustrate the use of correlation measurements to detect and quantify the development of active lava flow lobes on Kilauea volcano, Hawaii, first described by *Zebker et al.* [1996]. In this example interferometric radar data were acquired by the space shuttle imaging radar-C (SIR-C) on October 7-10, 1994. The site, located near the coast downslope from the Pu'u O'o vent, was imaged once per day, at about noon local time, on each of the four days. Maps of the correlation coefficient at each 15 m  $\times$  15 m resolution element of a 3840 m  $\times$  3840 m region exhibit the flows as regions of decorrelation (Plate 5).

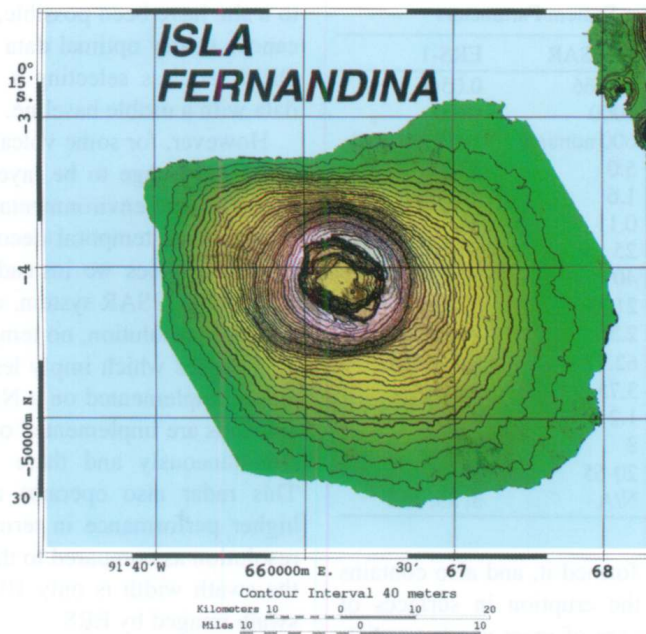


**Plate 4.** Contour map of Isla Fernandina, Galapagos Islands, derived from TOPSAR DEM. The contour interval is 40 m, the darker contours are spaced 200 m, and the brightness represents radar backscatter coefficient. This image consists of four parallel strips mosaicked together.

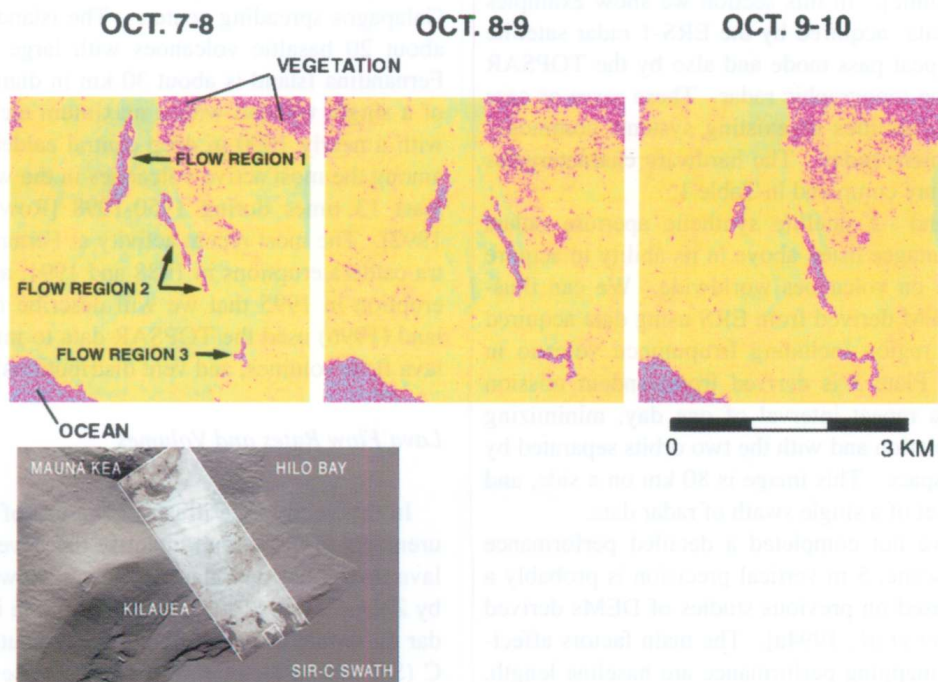


**Plate 5.** Correlation of Kilauea flows, located near the coast downslope from the Pu'u O'o vent. Interferometric radar data were acquired by the space shuttle imaging radar-C (SIR-C) on October 7-10, 1994. Maps of the correlation coefficient at each  $15 \text{ m} \times 15 \text{ m}$  resolution element of a  $3840 \text{ m} \times 3840 \text{ m}$  region exhibit the flows as regions of decorrelation. Inset small box shows location of area studied.

Active flows disturb the ground surface by burial of older landscapes, thus the radar echoes from these areas are essentially uncorrelated between radar observations. However, the surrounding areas can correlate quite well. Thus, the active flow regions may be discerned by plotting the correlation coefficient of the surface at each resolved point. The regions of decorrelation are seen to be grouped into three principal flows, as denoted by regions 1 to 3. The daily lava volume from each flow is obtained by assuming a flow thickness of 0.5 m, following field observations of the growing pahoehoe flow field concurrent with the radar observations. Although this is only an approximation, pahoehoe flows rarely exceed 1 m thick prior to inflation and are never less than ~20 cm thick [Hon *et al.*, 1994]. The surface breakouts originate from the same active flow field, so by combining the areas (and, by approximating the thickness of the flows, the volume) of new material one can derive an estimate of the mass eruption rate for this part of the volcano. Zebker *et al.* [1996] derived eruption rates of  $1.9 \text{ m}^3 \text{ s}^{-1}$ ,  $2.1 \text{ m}^3 \text{ s}^{-1}$  and  $2.1 \text{ m}^3 \text{ s}^{-1}$  for the three days. Such values are close to the  $\sim 3\text{--}4 \text{ m}^3 \text{ s}^{-1}$  cited by U. S. Geological Survey scientists making near-vent observations of the eruptions at Kilauea [Wolfe *et al.*, 1987; Mangan *et al.*, 1995]. The three independent volume estimates for the three days are very similar, which shows that the production rate of lava at Kilauea did not experience rapid fluctuations in lava production during the four days of observations.

These results illustrate not only the evolution of small lava flow fields at Kilauea, but indicate that similar analyses could identify areas of change associated with different types of pyroclastic volcanism. Examples might include activity associated with cinder cone formation, and possibly the deposition of pyroclastic materials formed by more explosive eruptions, where ash may be dispersed over many tens of square kilometers. Because field work in such areas of active volcanic can be expensive, time-consuming, logistically challenging, and dangerous for those involved, radar interferometry correlation observations offer the potential of greater insight into the magnitude and volcanic processes associated with each new eruption.

#### *Subsurface Dike Emplacement*

The final example illustrates how interpretation of crustal deformation data from an active volcano using geophysical inverse theory can help identify subsurface processes such as dike emplacement. The advantage of using interferometry is that it gives vastly more complete spatial coverage than conventional geodetic measurements. Using

this technique to study Fernandina Volcano, Galapagos, Jonsson *et al.* [1999] reported the observation of a dike intrusion. The radar data were acquired by ERS-1 and 2 over Fernandina in 1992 and 1997. Two interferograms were formed, an interferogram spanning the five years (Sept. 12, 1992–Sept. 30, 1997) and an interferogram that only spans one day (Sept. 29–30, 1997). The data in this study revealed strong localized uplift in a semi-circular pattern on the SW flank of the volcano at the site of a 1995 eruption (Plate 6). The spatially dense measurements enabled estimation of both the dimensions and the geometry of the dike using nonlinear inversion techniques.

The most recent activity at Fernandina includes intracaldera eruptions in 1988 and 1991 and a radial fissure eruption on the SW flank in 1995 [Wooster and Rothery, 1997; Global Volcanism Network, 1995]. The 1995 eruption began on around January 25 and lasted for about 10 weeks. The uppermost vents at elevations of 600–1100 m produced a negligible amount of lava. The main vent was located at 250 m elevation and produced about  $0.02 \text{ km}^3$  lava, assuming a 3 m average thickness [Wooster and Rothery, 1997]. The lava covered a subaerial area of  $8.2 \text{ km}^2$  extending 9 km from the uppermost vent to the ocean.

The five-year differential interferograms exhibit a strong semi-circular signal of range decrease on the SW flank of the volcano. The signal of more than 25 28-mm-fringes represents 0.75 m of decrease in range, that is, the ground moved towards the radar. Since the ERS SARs have an incidence angle of  $23^\circ$  from vertical this is presumably mainly uplift. The amplitude of the deformation pattern decreases from its maximum towards the caldera with a minimum at about 2 km from the caldera rim, where it increases again. This increase likely results from a second subsurface feature, but the incomplete nature of the signature due to decorrelation precludes simple analysis, hence an interpretation of the larger deformation pattern only is given below. Another, much smaller, semi-circular pattern is observed on the western side of the 1995 lava flow. This signal has an opposite sign, representing an increase in range of about two fringes, or about 0.06 m. A small deformation signal is also observed near the edges of the 1995 lava flow near the coast (Plate 6), probably representing subsidence due to the load of the new flows. The signal is of the order of one fringe, or an increase in range of 28 mm, over a subsidence zone that is less than 300 m wide.

The displacement at depth can be modeled using a single rectangular dislocation surface in an elastic half-space [Okada, 1985] to simulate ground deformation due to a dike intrusion, and a simulated annealing algorithm was used to help identify the global minimum in this nonlinear

interferogram shows deformation due to subsidence of the volcano during the 1995 eruption. This is indicated by the strong semi-circular signal of range decrease on the SW flank of the volcano, presumably mainly due to uplift. There is also a second subsurface feature near the crater rim. Another, much smaller, semi-circular, pattern is observed on the western side of the 1995 lava flow. The straight lines on the SW and NE coasts are not true topographic features but are due to incomplete TOPSAR coverage.

The differential interferogram shows the same deformation as the previous one but with more pronounced signals. The semi-circular signal on the SW flank has been replaced by a strong linear signal that extends from the crater rim to the SW coast. This may indicate new subsidence or inflation due to magma intrusion beneath the volcano. The semi-circular signal on the western side of the 1995 lava flow is also more pronounced. These strong subsidence features indicate that the volcano has subsided significantly since the previous measurement. The linear signal on the SW coast suggests that the volcano is still active and may be experiencing further subsidence or inflation.

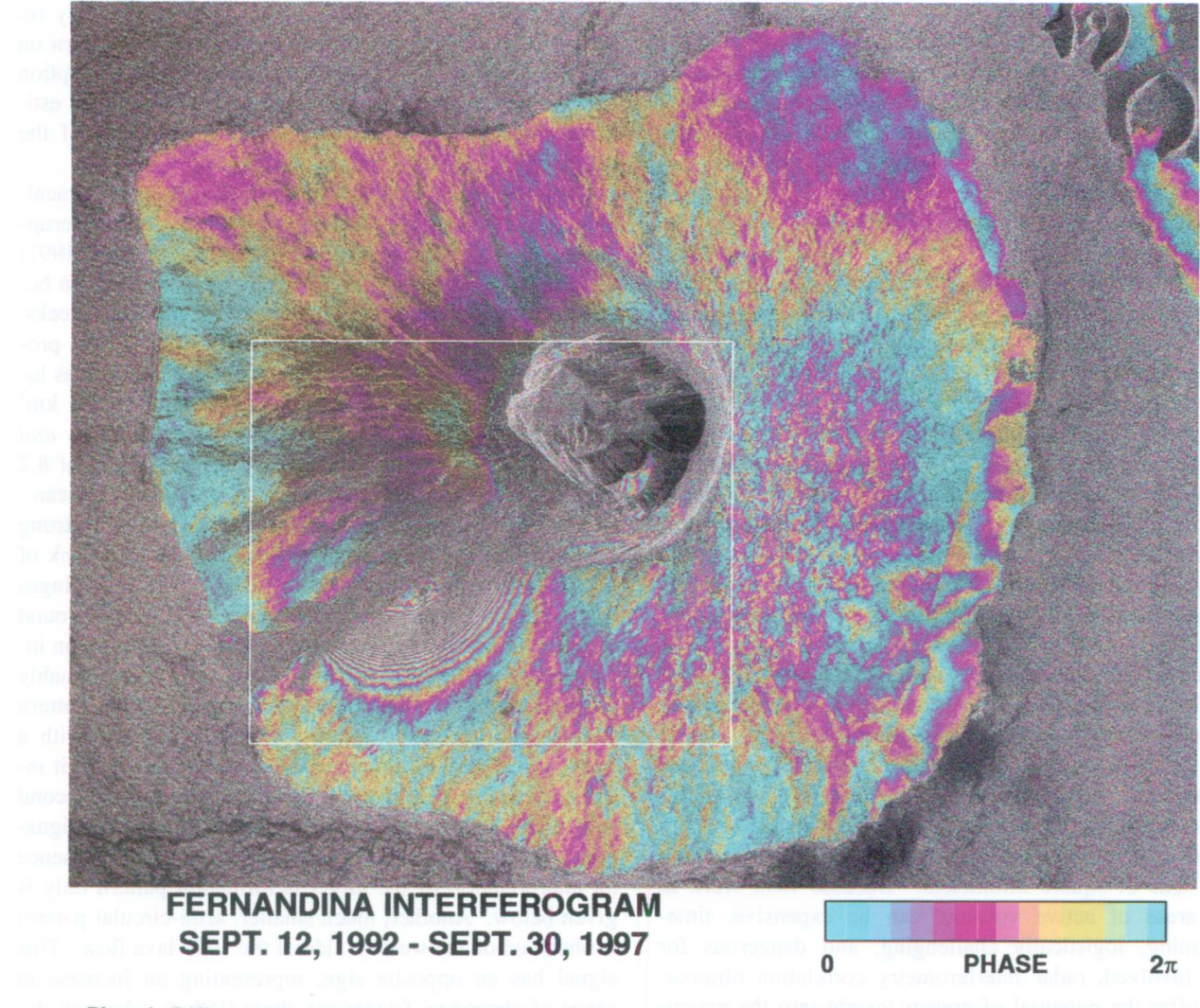


**Plate 6.** Differential interferogram of 1995 flank eruption on Fernandina, same field of view as Plate 4. This interferogram shows deformation that occurred during five years. The topographic signature was removed using the two-pass methods. The interferogram exhibits a strong semi-circular signal of range decrease on the SW flank of the volcano, presumably mainly due to uplift. There is also a second subsurface feature near the crater rim. Another, much smaller, semi-circular, pattern is observed on the western side of the 1995 lava flow. The straight lines on the SW and NE coasts are not true topographic features but are due to incomplete TOPSAR coverage.

problem [Cervelli *et al.*, 1997]. The best-fit model is a gently dipping dike, about 3.9 km long, 2.3 km high, 0.86 m thick, striking N47°E, and dipping 33° from horizontal to the SE. The inversion places the upper edge of the dike at the surface, coincident with where the eruption took place. The total dike volume ( $7.7 \times 10^3$  km $^3$ ) is ~40% of the volume of extrusive materials estimated to have been produced during the eruption [Wooster and Rothery, 1997]. Plate 7 shows the deformation in radar coordinates as predicted by the model; it matches the observations with less than 0.05 m residual over most of the signal. Sensitivity analysis of the inversion procedure using bootstrap techniques [Efron and Tibshirani, 1993] shows that the width of the 95% confidence interval is about 0.3 km for the dike length, 10° for the strike, 0.4 km for the dike depth, and 0.3 m for the dike opening. The dike dip and the dike height are less well constrained, at 18° and 1.0 km, respectively.

#### CASE STUDIES OF VOLCANOES IN DIFFERENT ENVIRONMENTS

The previous section illustrated specific studies of topographic change that can be conducted with radar interferometry, as well as the modeling of subsurface processes. Unfortunately not all volcanoes are as easily studied, because of the dependence of the quality on interferometric signals on both viewing geometry and the local physical environment. Hence observations of different volcanoes are of differing usefulness. One major limitation is temporal decorrelation due to either extreme environmental conditions such as rain and snow or to dense vegetation that can grow or move with time. Viewing geometry is also very important, as volcanoes often have very steep slopes leading to very high fringe rates, making it difficult to unwrap or otherwise interpret the phase signals.

In this section we present a summary of interferograms that we have acquired from many volcanoes around the world, located in many different environmental regions, with particular emphasis on the observed correlation properties of each. Our intent is to give some idea of how applicable the interferometry technique is in a variety of conditions and volcano types, and document cases (i) where we observe deformation, (ii) where we suspect deformation but cannot demonstrate it conclusively owing to poor data quality or quantity, (iii) where clearly no deformation occurs, and (iv) where no estimate could be made due to lack of coherence. We comment to what degree each may show usable phase signals that may be interpreted as deformation, in order to display both the utility and limitations of the technique. We have studied a large number of volcanoes from different environments that were active between

1992 and 1997 and imaged by the ERS1/2 SAR (Table 2, Figure 3). For completeness, the table also lists many of the volcanoes previously studied by others [see also *Massonnet and Sigmundsson*, this volume]—all of the results shown here are derived from ERS-1 and ERS-2 data. Most of the volcano case studies described in this paper were selected in summer 1997 based on the volcano activity reports of the Smithsonian Institution. Assuming data availability as reported in the ESA “DESCW” database there were for all of these volcanoes some chance to detect pre-eruptive and co-eruptive deformation. Unfortunately, many data acquisitions were not retrievable from the ESA archive because of malfunctions at a number of radar-downlink ground stations. Most of the problematic stations are located in regions of the world with less well-developed infrastructures, with attendant loss of reliability. It has been our experience that this situation has improved significantly since beginning of 1997. Some of the ground stations (for example, Cotopaxi, Ecuador) have received equipment upgrades which significantly improve their reliability.

Selected interferograms for each volcano are shown in Plates 8-11. For most volcanoes we also obtained differential interferograms by removing the topographic fringes. The differential interferograms are only shown for cases where we detected clear deformation (Plate 8). In most cases a short baseline (100-200 m) ERS 1-day tandem interferogram was used as the topographic interferogram. We include in Table 2 a summary of comments on the success or failure of interferometric techniques using C-band data as collected by ERS.

In the following discussion we focus on interferogram time periods targeting potential volcanic surface deformation, that is, the specific passes were selected because of reported activity at that volcano. Naturally, to obtain the differential interferograms we also produced for many volcanoes 1-day tandem interferograms that in principle could be used for DEM generation. The suitability of each volcano observation for DEM generation is also summarized in Table 2.

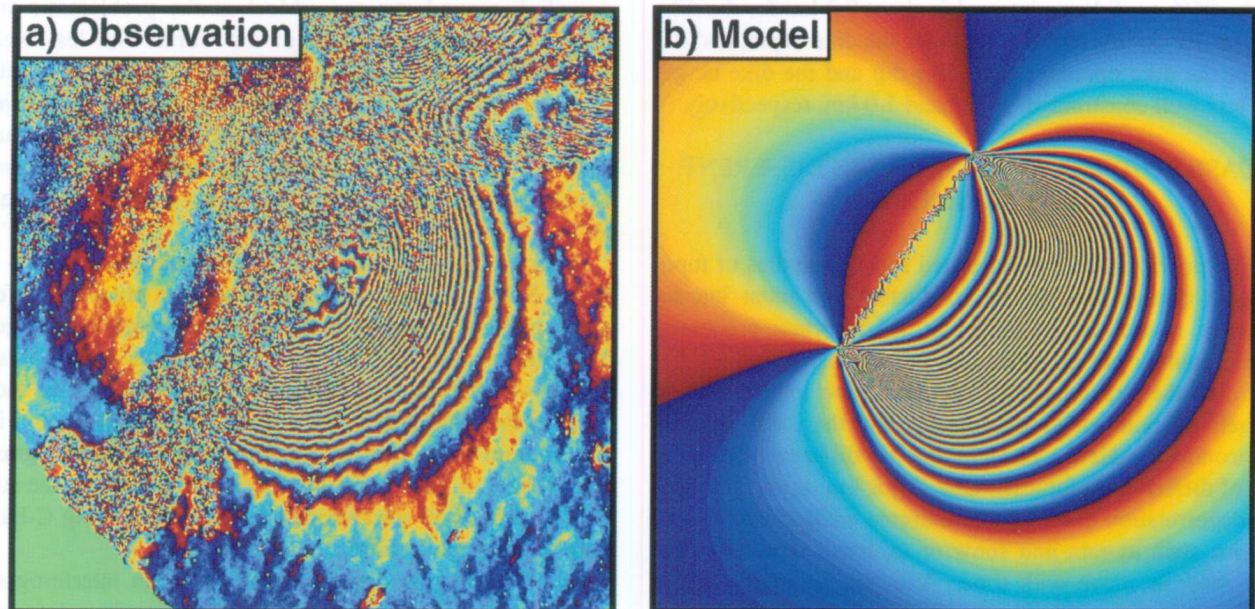
#### *Volcanoes Exhibiting Clear Deformation*

*Fogo, Cape Verde Islands* (Plate 8). Fogo erupted in April 1995 for the first time since 1951. The lava that now covers a major part of the summit caldera erupted from a fissure oriented S60°W [Fonseca *et al.*, 1998; Heleno and Fonseca, 1999]. The island is covered by old lava flows and has little vegetation. Many parts of the island maintain good coherence over a 2.5-year period covered by an interferogram. The co-eruptive surface deformation is depicted

**a) Observation**

This figure displays a grayscale map of wave patterns. The central region features concentric, roughly circular bands of alternating light and dark gray, representing wave crests and troughs. This pattern is set against a background that is heavily textured with small, irregular white speckles, suggesting noise or a complex underlying field. The overall shape of the wave pattern is roughly triangular, with the highest intensity of the concentric bands occurring near the top edge.

**Plate 7.** Deformation of Fernandina in radar coordinates a  
than 0.05 m residual over most of the signal. The best-fit  
high, 0.86 m thick, striking N47°E, and dipping 33° from E  
the dike at the surface, coincident with where the eruption



predicted by the model matches the observations with less than 10% error. The model is a gently dipping dike, about 3.9 km long, 2.3 km wide, and horizontal to the SE. The inversion places the upper edge of the dike at 1.5 km depth. The dip angle is 10°. The model has a vertical thickness of 1.5 km. The top surface of the dike is at 1.5 km depth. The bottom surface of the dike is at 3 km depth. The dike has a density of 2.6 g/cm<sup>3</sup>. The model has a vertical thickness of 1.5 km. The top surface of the dike is at 1.5 km depth. The bottom surface of the dike is at 3 km depth. The dike has a density of 2.6 g/cm<sup>3</sup>.

Table 2. Volcanoes Investigated Using Radar Interferometry

Site	Tandem DEM quality	Estimated maximum time period	References
<i>Previously published results:</i>			
1 Etna, Italy	good		<i>Massonnet et al.</i> , 1995; <i>Lanari</i> , 1998
2 Katmai, Alaska	---	2 yr (*)	<i>Lu et al.</i> , 1997
3 Krafla, Iceland	good	---	<i>Sigmundsson et al.</i> , 1997
4 Long Valley, California	n/a	3 yr	<i>Massonnet and Thatcher</i> , 1997
5 Okmok, Alaska	---	4 yr (*)	<i>Lu et al.</i> , 1998
6 Yellowstone, Wyoming	n/a	4 yr	<i>Wicks et al.</i> , 1998
7 Iwo Jima, Japan	poor	<2 yr	<i>Ohkura</i> , 1998 (JERS L-band)
8 Fernandina, Galapagos Islands	very good	5+ yr	<i>Jonsson et al.</i> , 1999
9 Piton de la Fournaise, Reunion	tbd	tbd	<i>Sigmundsson et al.</i> , 1999
<i>This paper, deformation seen: (Plate 8)</i>			
10 Fogo, Cape Verde	good	4 yr	
11 Akutan, Alaska	very bad	4 yr	
12 Gada Ale, Ethiopia	very good	5+ yr	
<i>This paper, possible deformation seen: (Plate 9)</i>			
13 Kuju, Japan	---	2 mo.	
14 Mayon, Phillipines	---	6 mo.(#)	
<i>This paper, interferogram shows no deformation: (Plate 10)</i>			
15 Irruputuncu, Chile	very good	2 yr (+)	
16 Popocatepetl, Mexico	o.k.	1 month	
17 Pacaya, Guatemala	bad	1 yr (#,+)	
18 Fuego, Guatemala	bad	5 mo. (#,+)	
19 Sakurajima, Japan	good	5 mo.	
<i>This paper, data quality too poor for reliable conclusion: (Plate 11)</i>			
20 Galeras, Columbia	---	6 mo. (#)	
21 Rincon de la Vieja, Costa Rica	---	1 yr (#,+)	
22 Merapi, Indonesia	bad	1 mo.	
23 Pavlof, Alaska	very bad	poor coherence	
24 Unzen, Japan & bad & poor coherence			
25 Souffriere Hills, Montserrat	very bad	no coherence	

*Explanation:*

## DEM quality:

- n/a not applicable, only two-pass analysis described  
 --- not known because no data exist, not available to us, or not given in references  
 very bad no coherence in most places  
 bad DEM generation possible for most of the volcano, typically except peak area  
 o.k. DEM generation possible, but errors likely due to unwrap problems, not useful for lahar and mud flow direction prediction  
 good good coherence, but DEM areas for some areas impossible because of foreshortening and layover related to the steep ERS look angle  
 very good very good coherence, same caveat as above

## Estimated maximum time period:

- not known because no data exist, not available to us, or not given in references  
 (\*) inferred from published papers  
 (+) inferred from our data covering longer or shorter time periods  
 (#) no coherence for most of the volcano's surface, but usable on lava flows -- could detect global volcano deformation  
 5+ 5 yr interferograms have very good coherence, coherence over longer time periods is expected

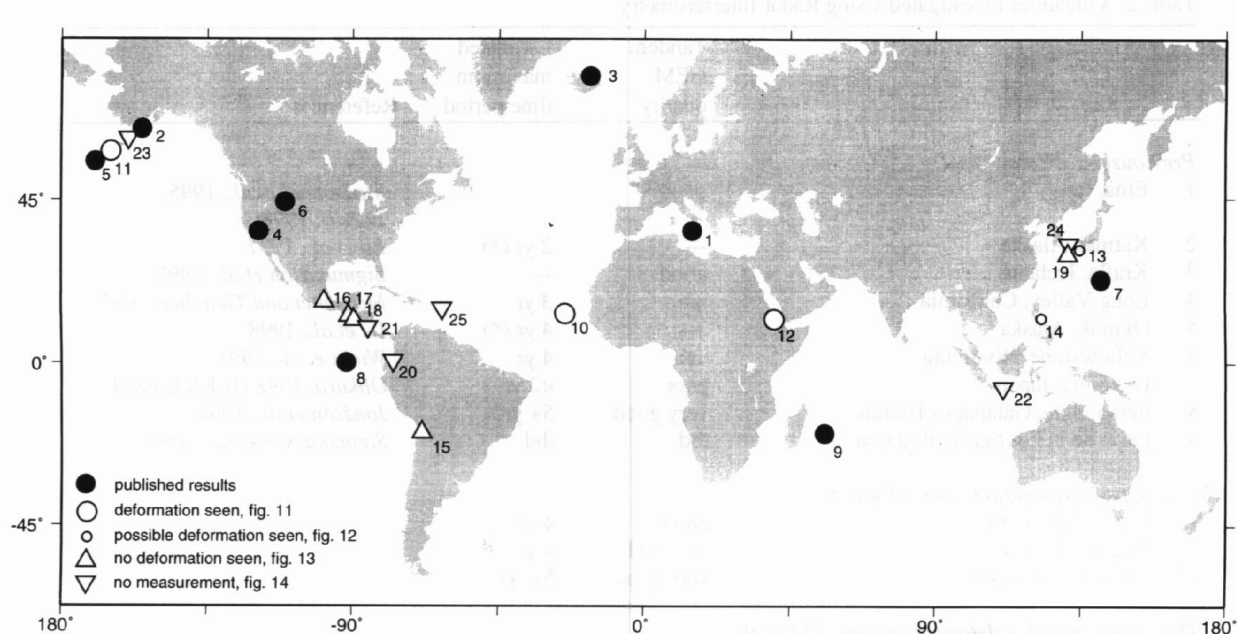


**Figure 3.** Map of location of volcanoes studied in this paper, with additional sites previously reported in the literature.

in a differential interferogram obtained after removing the topographic fringes using a 1-day tandem interferogram. About 3 fringes of range shortening (uplift) are observed. The fringe pattern, interrupted by many areas of non-coherence, appears to be consistent with a nearly vertical dyke with the same orientation as the eruptive fissure. It is interesting to note that the observed ground-deformation is smaller by a factor of about 5-10 than observed for dike intrusions at Fernandina and Piton de la Fournaise.

*Akutan, Alaska, USA* (Plate 8). Akutan Island was shocked by an earthquake swarm of volcano-tectonic origin with magnitudes of up to about 5.1 in March/April 1996. The earthquake swarm was not followed by a significant eruption but signs of increased eruptive activity during that period are reported by the Smithsonian Institution. Several ground cracks at the NW flank of the volcano are probably related to this period of seismic activity. A 2.1-year interferogram exhibits sufficient coherence for a ground deformation measurement over about half of the west flank of the volcano. The differential interferogram reveals a complicated pattern of deformation. A preliminary investigation indicates that most of the fringe pattern at the west flank of the volcano can be explained by the intrusion of a tilted dike. The deformation of the volcano was much more complex but will not be possible to retrieve because of a lack of coherence on the east flank of the volcano and in the summit area.

*Ertá Ale - Gada Ale, Ethiopia* (Plate 8). The Ertá Ale range is an 80-km-long basaltic shield volcano sitting on

top of the East African rift, where extension in direction perpendicular to the range axis is of the order of 0.8 cm per yr. The currently active volcano of the range is the Ertá Ale volcano. It has a lava lake in the summit caldera that currently changes level. A 4.3-year interferogram indicates that Ertá Ale is an excellent target for C-band interferometry. High coherence is maintained over the entire range. We formed a differential interferogram removing the topography using a 1-day tandem pair. No localized deformation was detected in the area of Ertá Ale volcano. However, we observe three fringes of range increase (subsidence) at the northwest end of the Ertá Ale range east of Gada Ale volcano. No earthquakes were reported during this period, indicating that the ground deformation may be aseismic deformation. It is interesting to note that the observed subsidence occurs in the area of lowest topography near and under Lake Karum, possibly indicating that this is the current area of active rifting.

#### *Volcanoes with Possible Deformation*

*Kuju, Japan* (Plate 9). The Kuju volcanic group on Kyushu island reawakened in October 1995 after 267 years of dormancy. A moderate eruption occurred over 2 months on a fissure on the north flank of Mt. Hosho. A 4-month interferogram covering the eruptive period has no (or little) coherence across the entire image except in a 2 km<sup>2</sup> area northwest of Mt. Hosho. The area to the south was covered by ash. About 1.5 fringes of range increase are

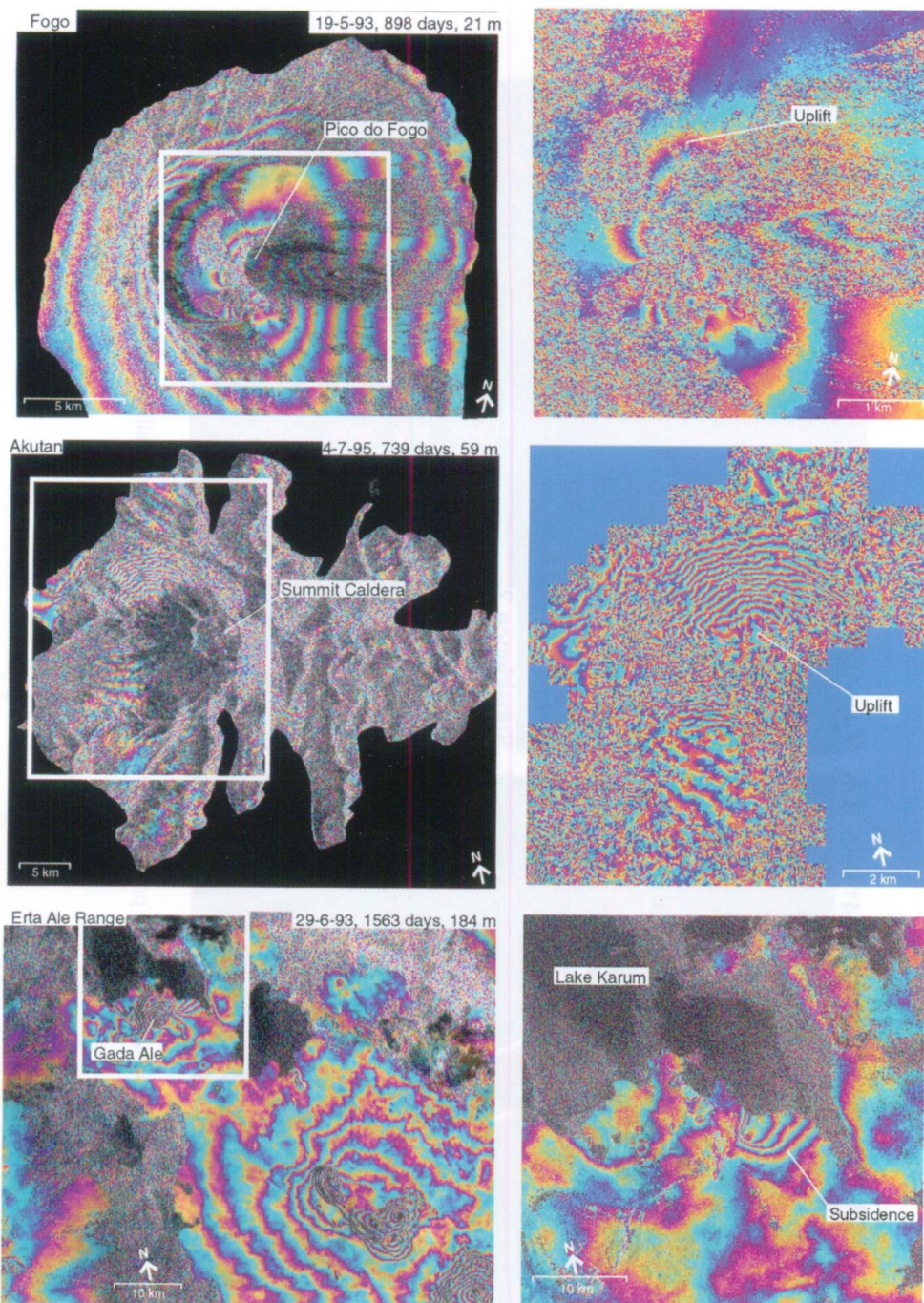


**Plate 8.** Interferograms of volcanoes exhibiting deformation: Fogo, Cape Verde Islands; Akutan, Alaska; and Gada Ale, Ethiopia. The name of each volcano is given in the upper left corner of the interferogram. The date of the first image, the time period for the pair, and the perpendicular baseline are given in the upper right. Right-hand column shows enlargements of white boxes seen at left, and display phase information only. One cycle of phase is represented by one color fringe. The elevation difference represented by one fringe depends on perpendicular baseline (see text), while one fringe in the case of surface deformation represents 2.8 cm of range change. All interferograms here and in subsequent figures are shown in radar coordinates. Actual shapes and scale may be different because of foreshortening and shadowing effects.

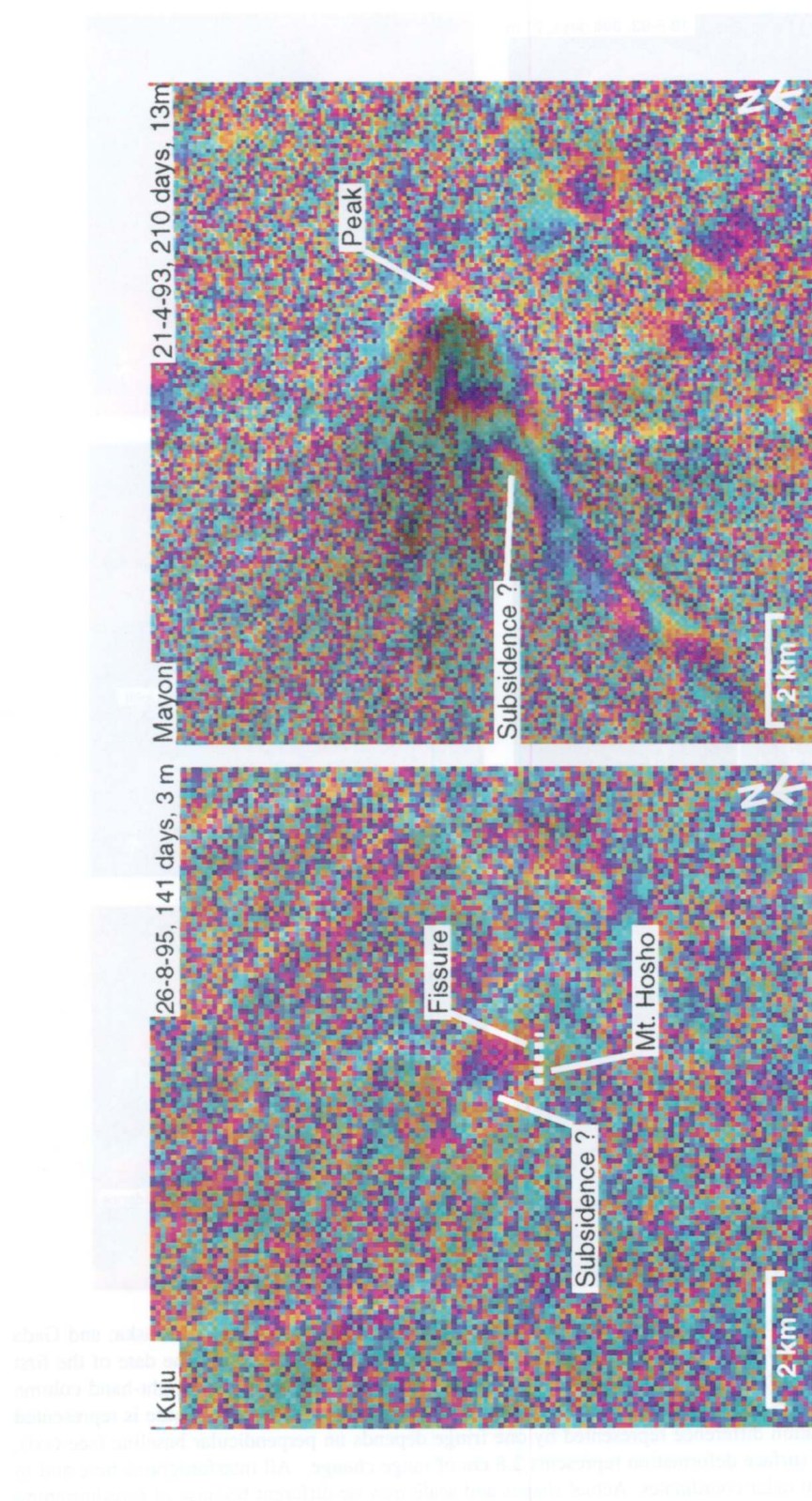


Plate 9. Interferograms of volcanoes with possible deformation: Kuju, Japan, and Mayon, Philippines. Ancillary data as in Plate 8.

detected in this area, probably indicating subsidence of about 4 cm. By comparison with a tandem interferogram we verified that this is not a topographic residual. The phase signature could in principle also be due to atmospheric water vapor. We were not able to exclude this possibility because interferograms covering a similar time period decorrelate in this area. The interferogram of a small portion of the scene is shown, but several coherent patches primarily over urban areas give us some idea about the tropospheric conditions during the time of the image acquisitions. Those phase signatures are completely different than those visible over the volcanic terrain. This makes us reasonably confident that deformation is present. In the same area about 7 cm of range increase was detected with JERS interferometry (M. Shimada, personal communication), and about 20 cm of slope distance change with electronic distance measurements (EDM) [Sudo *et al.*, 1998]. The results shown here are the ERS results.

*Mayon, Philippines* (Plate 9). Mayon erupted in February–March 1993. We produced an interferogram covering a 7-month period starting about 1 month after the end of the eruption. Over this time period some coherence is maintained on the west and in particular on the southwest flanks of the volcano, indicating that deformation measurements with interferograms covering more than half a year are in principle possible with C-band interferometry. A portion of a presumably circular phase signature indicating a range increase (subsidence) is visible on the southwest flank of the volcano that may be the result of a collapse or compaction of the magma chamber during the eruption. No additional data exist to exclude an atmospheric disturbance as the source for the phase signature. As in the earlier example at Kuju inspection of coherent patches across the entire interferogram revealed that the size and presumably circular pattern of this phase signature are not typical for tropospheric signatures, making deformation the most likely cause for the phase signature.

#### *Volcanoes Showing no Deformation*

*Irruputuncu* (Plate 10). The Smithsonian Institution volcanic activity reports indicate that Irruputuncu has produced ash emissions on 1 September and 26 November 1995. A 70-day interferogram covering the 1 September 1995 activity shows a high level of coherence, suggesting that interferometric deformation measurements can be made with interferograms covering several years. We obtained a differential interferogram over this period of activity but no deformation was detected. If there were significant (>1-2 cm) deformation then it would be detectable

in our data. Hence, the ash emissions apparently were not accompanied by surface deformation in this instance.

*Popocatepetl* (Plate 10). We obtained interferometric data for the period just before the eruption of 30 April 1996. A 70-day interferogram shows coherence over about one third of the volcano. Because of extreme foreshortening and layover, the flank of the volcano in direction of the radar is not imaged. A differential interferogram (not shown) showed a small localized phase signature that may represent deformation; however, it also may be an atmospheric disturbance in one of the images. It could also be related to the emission of gas that raises the dielectric constant of the atmosphere for one of the images. These could only be distinguished using several images covering this time period using the pair-wise logic outlined by Feigl *et al.* [1995]. In this case, however, this is not possible because no more data exist. We obtained also two 1-day tandem interferograms of the area. In one tandem interferogram from April 96 the fringes are less clear than in another 1-day interferogram from December 1995. This is somewhat surprising since we expect less coherence owing to greater snow coverage for the December pair than for the April pair. The lower coherence in April may be because of a small ash emission between the two image acquisition times preceding the April 30 eruption, although none was reported. The coherence in the April tandem interferogram is too low for reliable automatic phase unwrapping.

*Pacaya* (Plate 10). Pacaya erupted on 1 June 1995 and on 11 November 1996. We obtained an interferogram for the period from December 1995 to April 1996, spanning about one-fourth of the inter-eruptive period. No deformation in the radar-coherent portions of the volcano was detected during this time period. The interferogram exhibits high coherence over the south flank of the volcano, an area probably covered by recent (historic) lava flows with very little vegetation. This is encouraging and suggests that sufficient coherence to detect a global deformation of the volcano related to the intrusion or extrusion of magma into a magma chamber is maintained over periods of 1 year or so.

*Fuego* (Plate 10). Activity at Fuego, located about 30 km to the west of Pacaya, was reported for November 1996. Fuego is covered by the same SAR acquisition as Pacaya. No deformation was detected between December 1995 and April 1996. High coherence is maintained over a much smaller area than at Pacaya. It is interesting that a high coherence area exists in the summit area where most other volcanoes lose coherence. A narrow high coherence area on the east flank of Fuego extends from the summit to

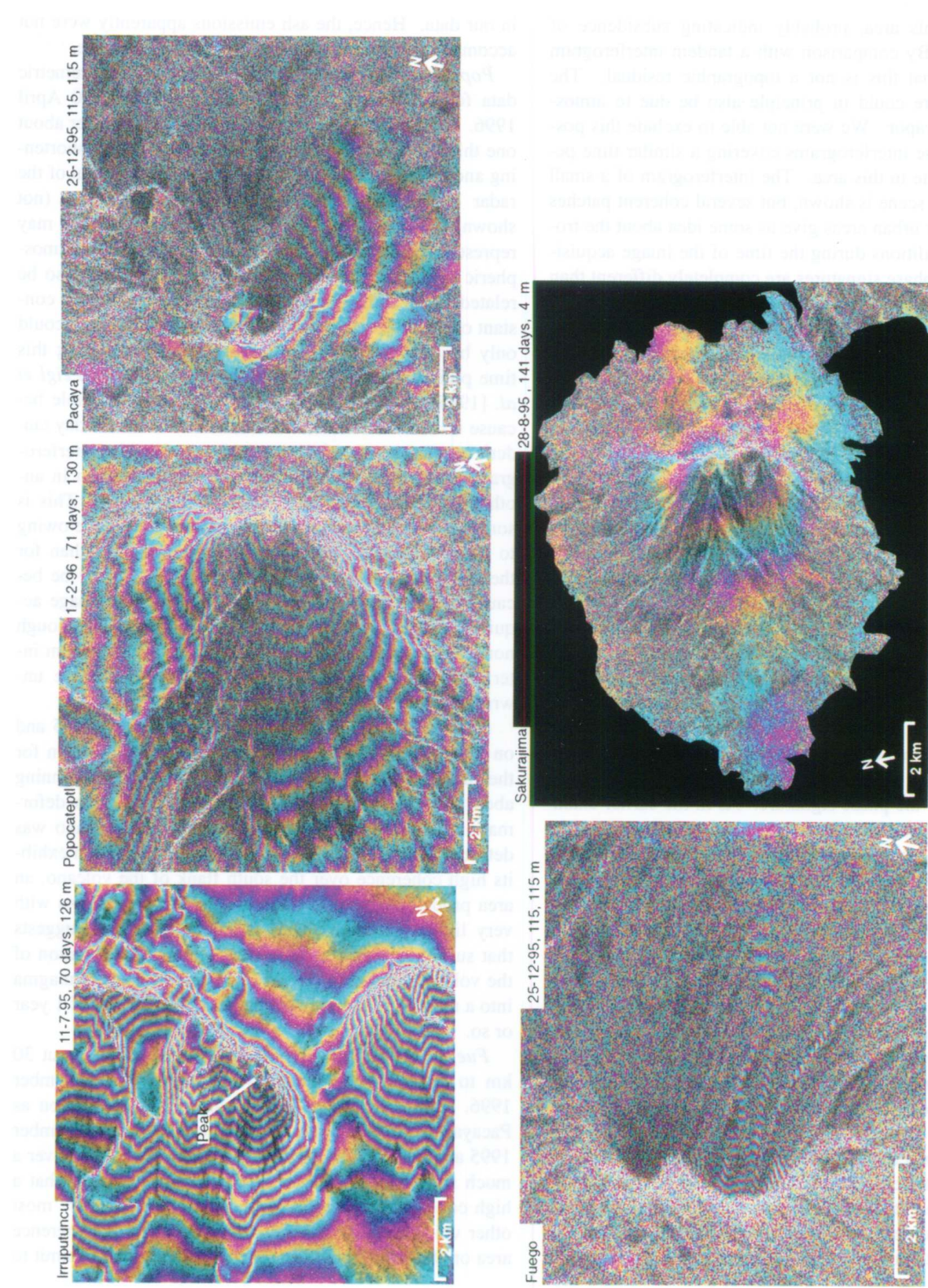


Plate 10. Interferograms of volcanoes showing no deformation: Irruputuncu, Chile; Popocatepetl, Mexico; Pacaya, Guatemala; Fuego, Guatemala; and Sakurajima, Japan. Ancillary data as in Plate 8.

the foot of the volcano and suggests that a global deformation may be detectable. The high coherence area is probably confined to a recent lava flow.

*Sakurajima* (Plate 10). Here we obtained interferometric data over the time period July 1995 to February 1996. This period was relatively well covered by about 8 interferograms with temporal intervals between 70 and 280 days. Sakurajima interferograms maintain relatively high coherence for a period up to 140 days. For periods of up to one year some coherence is maintained over most parts of the volcano, so that in principle deformation of 2 cm or more can be detected. However, our results indicate that no such deformation occurred. It is questionable whether such deformation is expected since Sakurajima is probably fed from a deep magma chamber in the center of Aira caldera [Dvorak and Dzurisin, 1997].

#### *Volcanoes With Data Quality too Poor for Reliable Analysis*

*Galeras* (Plate 11). We attempted to study the eruptive period of January to June 1993. For Galeras, archive reliability was an issue. Although many images covering this time period were listed as available they could not be delivered and we obtained only one interferogram. This is a practical limitation of existing data which should improve as future systems become more reliable. Some coherence is maintained on the NW flank of the volcano. This was surprising to us because we expected ash emissions during the eruption to change the surface significantly. The result indicates that the conditions for interferometric measurements at Galeras are not ideal but the situation is not hopeless. With dense temporal coverage interferometric analyses could indeed contribute to the monitoring of this volcano.

*Rincon de la Vieja* (Plate 11). We attempted to study the eruptive periods of November 1995. We were able to generate only one 35-day interferogram; as with Galeras, archive reliability was an issue. Most of the volcano's surface does not maintain coherence over this period, probably because of the dense vegetation cover. A lava flow on the south flank of the volcano, however, maintains very high coherence over this period. It is likely that the lava flow would maintain coherence over a period of 1 year or longer, indicating that with good data coverage a global inflation or deflation of the volcano could be detected with interferometric techniques.

*Merapi* (Plate 11). We examined a 70-day interferogram for the period 10 June to 16 August 1996. No coherence is seen on the flanks of the volcano. This may be directly related to volcanic activity. According to the Smithsonian Institution reports on August 9, 1996, a pyroclastic

flow traveled for 3.5 km on the SSW flank of the volcano from the summit downhill. Related ash falls may have changed the volcano's surface and hence the radar backscatter characteristics. It is encouraging that some coherence is maintained at the foot of the volcano. The coherent signal is probably backscattered from bare, burned, surfaces and the many villages around the volcano. With signals observed around the base of the volcano, it may be possible with InSAR to detect deformation related to a deep magma chamber, if such a chamber exists.

*Pavlof* (Plate 11). Pavlof is one of the most active Alaskan volcanoes. It last erupted in Fall 1996. A 35-day interferogram is shown. The summit area decorrelates completely, perhaps owing to snow still covering the volcano at end of July 1993. This interferogram illustrates well the problem of observing Pavlof with ERS interferometry. We also made several 4-year interferograms covering the eruption of 1996 (not shown) that showed a similar pattern of correlated and decorrelated areas.

*Unzen, Japan* (Plate 11). Unzen was in eruption from 1990 to 1995. We intended to study the eruption since 1992-1993 eruptive period. A 70-day interferogram shows that C-band interferometry cannot contribute much to monitor ground deformation at Unzen. Coherence is maintained only at a small portion of the north flank of the volcano. We made other, longer time-spanning interferograms where the coherence in the volcano area was essentially zero.

*Montserrat* (Plate 11). Montserrat turned out to be very difficult to analyze with interferometric methods, at least for C-band interferometry. A 35-day pair during the current eruption at Souffriere Hills exhibits very low coherence except from small localized areas on the coast in the north part of the island, an area that is little affected by emissions from Souffriere Hills. We did obtain several 1-day tandem interferograms; our intent was to difference digital elevation models in order to map large surface changes of the volcano, such as dome growth. The coherent areas visible in the tandem interferograms are only slightly larger than in the 35-day interferogram, still too small for geophysically useful results.

#### CONCLUSIONS

Radar interferometric techniques have proven valuable for remote sensing studies of volcanoes. Precise topographic measurements, the ability to monitor surface cover changes from active lava flows, and resolution of extremely small deformations of the surface over large areas all give information about volcanoes that is difficult if not impossible to obtain otherwise. These detailed measurements of surface processes may be further analyzed to infer

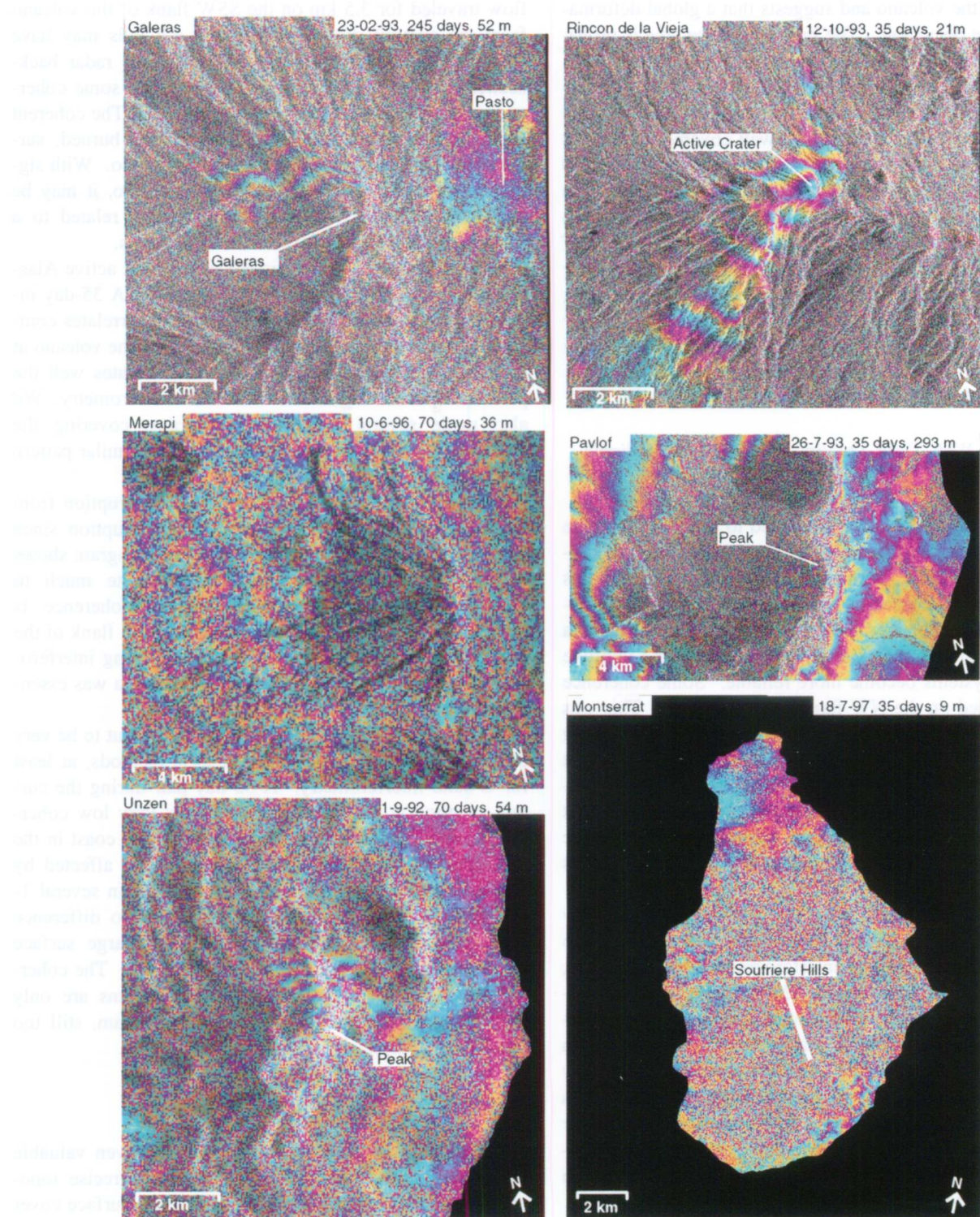


**Plate 11.** Interferograms of volcanoes with data quality too poor for reliable analysis: Galeras, Colombia; Rincon de la Vieja, Costa Rica; Merapi, Indonesia; Pavlof, Alaska; Unzen, Japan; and Soufriere Hills, Montserrat. Ancillary data as in Plate 8.

volume or other changes at depth and thus to provide a window through which to view subsurface activity. All this is possible on a global basis from orbiting satellites, making it feasible now to monitor hazards from the world's 600 or so active volcanoes.

Interferometric radar measurements of crustal deformation on an active volcano using geophysical inverse theory can help identify subsurface processes such as dike emplacement and better explain the inner workings of a volcano. The advantage of using interferometry here is that it gives much more complete spatial coverage than conventional geodetic measurements. Spatially dense measurements enable us to determine both the dimensions and the geometry of dislocation at depth using nonlinear inversion techniques. In addition to solutions for intrusion location and geometry, these analyses can yield new and unexpected information about the stress field of volcanoes. In the case of Fernandina, geological investigations show that vents and presumably underlying dikes on the caldera rim have an arcuate, caldera-parallel orientation, but vents further away from the rim are radial. The radar measurements allow us to determine the minimum compressional stress axis, for the emplaced dike rotates in the horizontal plane about the vertical axis, and also about the horizontal axis, at least at shallow depths. Such insights into the stress fields of volcanoes can greatly change the way we envision their structure and evolution.

We have found that the best targets for radar interferometry are shield volcanoes and large calderas, at least when the principal source of data is the ERS satellites. Stratovolcanoes appear to be less suited for radar interferometric observations owing to large geometric distortions and severe environmental conditions near the summits. These majestic volcanoes are characterized by steep topography; thus foreshortening and layover are serious problems and constrain the analysis of interferometric data. Some are so high that the peaks are snow- and ice-covered, at least seasonally if not year-round, resulting in a loss of coherence over the most interesting parts of the volcano. As shown in the analysis of the Fernandina 1995 eruption, fissure eruptions on a flank of a volcano, however, are amenable to observation as the topographic relief is less and the lower altitude leads to milder climates. This result implies that even the stratovolcanoes may be analyzed if we examine these events that occur lower down the peak.

Regarding the reliability of the technique, radar interferometry using the ERS-1 and ERS-2 satellites can be used for the monitoring of certain volcanoes with particular conditions where the above restrictions do not apply. Examples include Etna, Fogo, and Fernandina. For many other volcanoes, however, in particular stratovolcanoes,

ERS C-band interferometry has only very limited use. We stress that even ERS interferometry, though, has significantly broadened our knowledge about how volcanoes work and how the intrusion and extrusion of magma causes the volcano surface to deform.

Future satellite missions could be designed to optimized volcano study. Using greater incidence angles would eliminate much of the problem with geometric distortion related to steep topography, and the use of longer wavelengths such as L-band (24 cm) lessens the issue with temporal decorrelation. Frequent observations and short revisit periods can better constrain the time of occurrence of an event and aid in operational readiness. Radar analyses with their improved model constraints will impact our ability to forecast impending eruptions and thus benefit society worldwide.

**Acknowledgments.** We would like to acknowledge NASA for providing SIR-C/XSAR and TOPSAR data, and the European Space Agency for providing ERS-1 and -2 data, without which the above analyses would have been impossible. Falk Amelung was partially supported under a contract with ESA, the remainder of this work was supported under contract to NASA and NSF. We would also like to thank Mark Simons, Pete Mouginis-Mark, and one anonymous reviewer for many helpful comments in assembling this manuscript.

## REFERENCES

- Amelung, F., D. L. Galloway, J. W. Bell, H. A. Zebker, and R. J. Lacziak, Sensing the ups and downs of Las Vegas: InSAR reveals structural control of land subsidence and aquifer-system deformation, *Geology*, 27, 483–486, 1999.
- Cervelli, P., P. Segall, and Y. Aoki, Simulated annealing for inverting surface displacements for fault slip and geometry, with an application to the 1994 earthquake swarm off the Izu Peninsula of Japan (abstract), *Eos Trans. AGU*, 78, 159, 1997.
- Chadwick, W. W., Jr., and J. H. Dieterich, Mechanical modeling of circumferential and radial dike intrusion on Galapagos volcanoes, *J. Volcanol. Geotherm. Res.*, 66, 37–52, 1995.
- Curlander, J., and R. N. McDonough, *Synthetic Aperture Radar, Systems and Signal Processing*, John Wiley & Sons, Inc., New York, 1991.
- Dixon, T., (Ed.), Land Processes DAAC Science Advisory Panel, Topographic data requirements for EOS global change research, NASA Publication, 1994.
- Dvorak, J. J., and D. Dzurisin, Volcano geodesy; the search for magma reservoirs and the formation of eruptive vents, *Rev. Geophys.*, 35, 343–384, 1997.
- Efron, B. and R. J. Tibshirani, *Introduction to the Bootstrap, Monographs on Statistics and Applied Probability*, 57, Chapman and Hill, New York, 1993.
- Elachi, C., *Spaceborne radar remote sensing: applications and techniques*, Institute of Electrical and Electronics Engineers, New York, 1988.

- Evans, D. L., T. G. Farr, H. A. Zebker, and P.J. Mouginis-Mark, Radar interferometric studies of the Earth's topography, *Eos Trans. AGU*, 73, 553, 557–558, 1992.
- Feigl, K. L., A. Sergeant, and D. Jacq, Estimation of an earthquake focal mechanism from a satellite radar interferogram; application to the December 4, 1992 Landers aftershock, *Geophys. Res. Lett.*, 22, 1037–1040, 1995.
- Fonseca, J. F. B. D., S. J. Day, J. L. G. Matos, J. N. P. Lima, A. Berberan, S. I. N. Heleno, F. Amelung, and N. d'Oreye, Ground deformation monitoring in the Fogo Volcano, Cape Verde Islands, Compte Rendus of the 83rd Journees Luxembourgeoises de Geodynamique, G.D. Luxembourg, March 1998.
- Gabriel, A. K., R. M. Goldstein, and H. A. Zebker, Mapping small elevation changes over large areas: differential radar interferometry, *J. Geophys. Res.*, 94, 9183–9191, 1989.
- Gatelli, F., A. Monti Guarneri, F. Parizzi, P. Pasquali, C. Prati, and F. Rocca, The wavenumber shift in SAR interferometry, *IEEE Trans. Geosci. Rem. Sens.*, 32, 855–65, 1994.
- Ghiglia, D. C., and L. A. Romero, Robust two-dimensional weighted and unweighted phase unwrapping that uses fast transforms and iterative methods, *J. Opt. Soc. Am.*, 11, 107–117, 1994.
- Global Volcanism Network, *Smithsonian Inst. Bull.* 20(1)–20(5), 1995.
- Goldstein, R. M., H. A. Zebker, and C. Werner, Satellite radar interferometry: two-dimensional phase unwrapping, *Radio-science*, 23, 713–720, 1988.
- Graham, L. C., Synthetic interferometer radar for topographic mapping, *Proc. IEEE*, 62, 763–768, 1974.
- Gray, A. L., and P. J. Farris-Manning, Repeat pass interferometry with airborne synthetic aperture radar, *IEEE Trans. Geosci. Remote Sens.*, 31, 180–191, 1993.
- Heleno, S. I. N., and J. F. B. D. Fonseca, A seismological investigation of Fogo Volcano: preliminary results, *J. Volcanol.*, in press, 1999.
- Hon, K., J. Kauahikaua, R. Denlinger, and K. MacKay, Emplacement and inflation of pahoehoe sheet flows: Observations and measurements of active lava flows on Kilauea volcano, Hawaii, *Geol. Soc. Am. Bull.*, 106, 351–370, 1994.
- Iverson, R. M., S. P. Schilling, and J. W. Vallance, Objective delineation of lahar-inundation hazard zones, *Geol. Soc. Am. Bull.*, 110, 972–984, 1998.
- Jonsson, S., H. Zebker, P. Cervelli, P. Segall, H. Garbeil, P. Mouginis-Mark, and S. Rowland, A shallow-dipping dike fed the 1995 flank eruption at Fernandina volcano, Galapagos, observed by satellite radar interferometry, *Geophys. Res. Lett.*, 26, 1077–1080, 1999.
- Lanari, R., P. Lundgren, and E. Sansosti, Dynamic deformation of Etna volcano observed by satellite radar interferometry, *Geophys. Res. Lett.*, 25, 1541–1544, 1998.
- Langbein, J. O., D. P. Hill, T. N. Parker, and S. K. Wilkinson, An episode of reinflation of the Long Valley Caldera, eastern California; 1989–1991, *J. Geophys. Res.*, 98, 15,851–15,870, 1993.
- Li, F., and R. M. Goldstein, Studies of multi-baseline spaceborne interferometric synthetic aperture radars, *IEEE Trans. Geosci. Rem. Sens.*, 28, 88–97, 1990.
- Lu, Z., R. Fatland, M. Wyss, S. Li, J. Eichelberger, K. Dean, and J. Freymueller, Deformation of New Trident Volcano measured by ERS 1 SAR interferometry, Katmai National Park, Alaska, *Geophys. Res. Lett.*, 24, 695–698, 1997.
- Lu, Z., D. Mann, and J. Freymuller, Satellite radar interferometry measures deformation at Okmok volcano, *Eos Trans. AGU*, 79, 461, 467, 1998.
- Madsen, S. N., J. Martin, and H. A. Zebker, Analysis and evaluation of the NASA/JPL TOPSAR interferometric SAR system, *IEEE Trans. Geosci. Rem. Sens.*, 33, 383–391, 1995.
- Mangan, M. T., C. C. Heliker, T. N. Mattox, J. P. Kauahikaua, and R. T. Helz, Episode 49 of the Pu'u 'O'o-Kupaianaha eruption of Kilauea volcano—breakdown of a steady-state eruptive era, *Bull. Volcanol.*, 57, 127–135, 1995.
- Massonnet, D., M. Rossi, C. Carmona, F. Adragna, G. Peltzer, K. Feigl, and T. Rabaute, The displacement field of the Landers earthquake mapped by radar interferometry, *Nature*, 364, 138–142, 1993.
- Massonnet, D., P. Briole, and A. Arnaud, Deflation of Mount Etna monitored by spaceborne radar interferometry, *Nature*, 375, 567–570, 1995.
- Ohkura, H., Application of SAR data to monitoring Earth surface changes and displacement, *Adv. Space Res.*, 21, 485–492, 1998.
- Okada, Y., Surface deformation due to shear and tensile faults in a half-space, *Bull. Seismol. Soc. Am.*, 75, 1135–1154, 1985.
- Rowland, S. K., Slopes, lava flow volumes, and vent distributions on Volcan Fernandina, Galapagos Islands, *J. Geophys. Res.*, 101, 27,657–27,672, 1996.
- Rowland, S. K., and D. C. Munro, The caldera of Volcan Fernandina; a remote sensing study of its structure and recent activity, *Bull. Volcanol.*, 55, 97–109, 1992.
- Sigmundsson, F., H. Vadon H. and D. Massonnet, Readjustment of the Krafla spreading segment to crustal rifting measured by satellite radar interferometry, *Geophys. Res. Lett.*, 24, 1843–1846, 1997.
- Sigmundsson, F., P. Durand, and D. Massonnet, Opening of an eruptive fissure and seaward displacement at Piton de la Fournaise volcano measured by RADARSAT satellite radar interferometry, *Geophys. Res. Lett.*, 26, 533–536, 1999.
- Sudo, Y., and 16 others, Seismic activity and ground deformation associated with 1995 phreatic eruption of Kuju Volcano, Kyushu, Japan, *J. Volcanol. Geotherm. Res.*, 81, 245–267, 1998.
- Wicks, C. W., W. Thatcher, and D. Dzurisin, Migration of fluids beneath Yellowstone Caldera Inferred from satellite Radar interferometry, *Science*, 282, 458–462, 1998.
- Wolfe, E. W., M. O. Garcia, D. B. Jackson, J. Koyanagi, C. A. Neal, and A. T. Okamura, The Pu'u 'O'o eruption of Kilauea volcano, episodes 1–20, January 3, 1983 to June 8, 1984, in *Volcanism in Hawaii, U.S. Geol. Surv. Prof. Paper 1350*, edited by R. W. Decker, T. L. Wright, and P. H. Stauffer, pp. 471–508, 1987.
- Wooster, M. J. and D. A. Rothery, Time-series analysis of effusive volcanic activity using the ERS Along Track Scanning Radiometer: the 1995 eruption of Fernandina Volcano, Galapagos Islands, *Remote Sens. Environ.*, 62, 109–117, 1997.
- Zebker, H., and R. Goldstein, Topographic mapping frominterferometric SAR observations, *J. Geophys. Res.*, 91, 4993–4999, 1986.

- Zebker, H. A., and J. Villasenor, Decorrelation in interferometric radar echoes, *IEEE Trans. Geosci. Rem. Sens.*, 30, 950–959, 1992.
- Zebker, H. A., S. N. Madsen, J. Martin, K. B. Wheeler, T. Miller, Y. Lou, G. Alberti, S. Vettrella, and A. Cucci, The TOPSAR interferometric radar topographic mapping instrument, *IEEE Trans. Geosci. Rem. Sens.*, 30, 933–940, 1992.
- Zebker, H.A., C.L. Werner, P. Rosen, and S. Hensley, Accuracy of topographic maps derived from ERS-1 radar interferometry, *IEEE Trans. Geosci. Rem. Sens.*, 32, 823–836, 1994a.
- Zebker, H. A., P. A. Rosen, R. M. Goldstein, A. Gabriel, and C. Werner, On the derivation of coseismic displacement fields using differential radar interferometry: the Landers earthquake, *J. Geophys. Res.*, 99, 19,617–19,634, 1994b.
- Zebker, H. A., P. A. Rosen, S. Hensley, and P. Mouginis-Mark, Analysis of active lava flows on Kilauea volcano, Hawaii, using SIR-C radar correlation measurements, *Geology*, 24, 495–498, 1996.
- Zebker, H.A., P.A.Rosen, and S. Hensley, Atmospheric effects in interferometric synthetic aperture radar surface deformation and topographic maps, *J. Geophys. Res.*, 102, 7547–7563, 1997.
- Zebker, H.A., and Y. Lu, Phase unwrapping algorithms for radar interferometry: residue/cut, least-squares, and synthesis algorithms, *J. Opt. Soc. Am.*, 5, 586–598, 1998.
- 
- F. Amelung, S. Jonsson, and H. A. Zebker, Departments of Geophysics and Electrical Engineering, Stanford University, Stanford, CA 94305-9515. (e-mail: zebker@stanford.edu)